Strain Mapping of Single Nanowires using Nano X-ray Diffraction

Hammarberg, Susanna

2023

Document Version:
Publisher's PDF, also known as Version of record

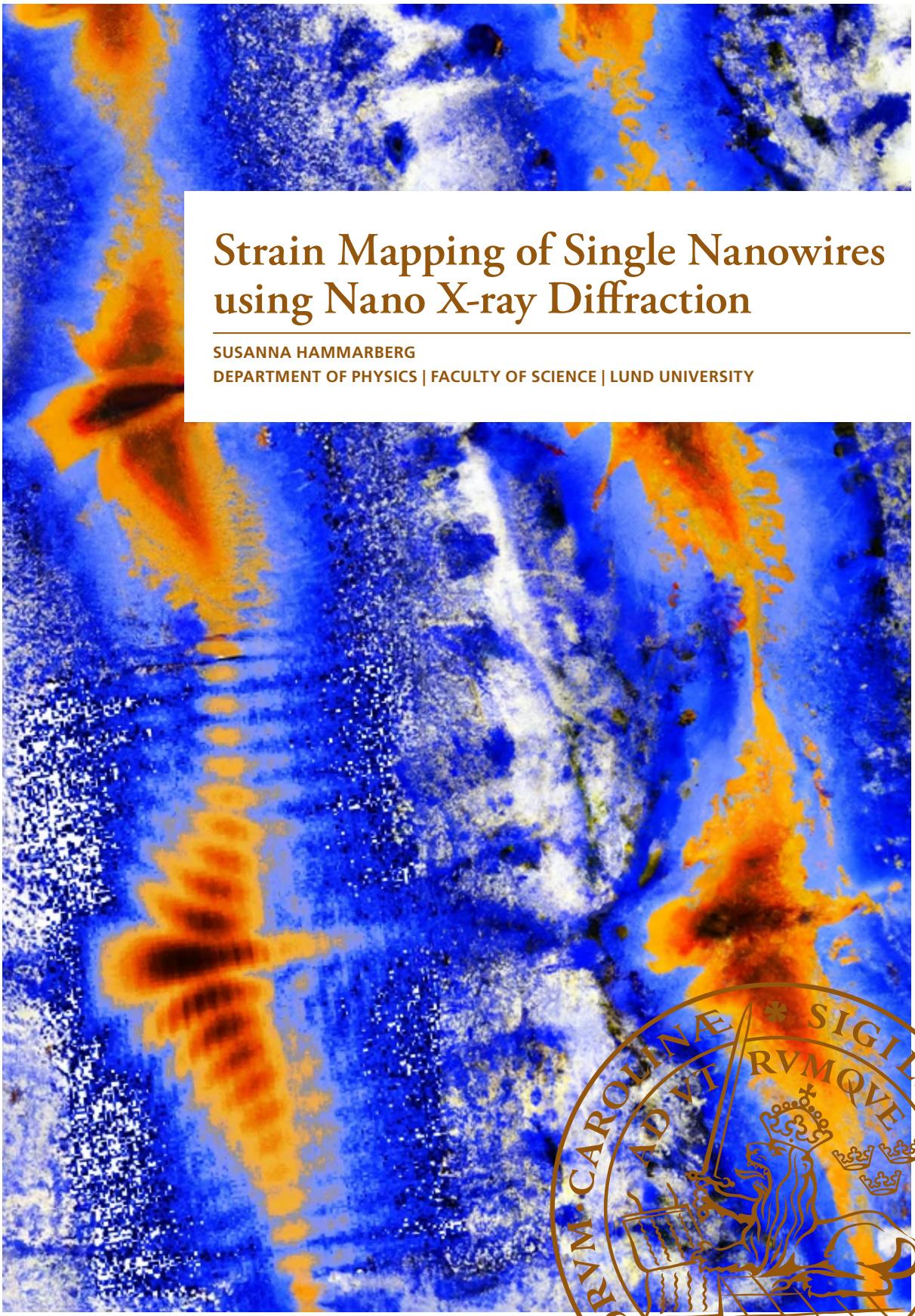

Strain Mapping of Single Nanowires using Nano X-ray Diffraction

SUSANNA HAMMARBERG
DEPARTMENT OF PHYSICS | FACULTY OF SCIENCE | LUND UNIVERSITY

Strain Mapping of Single Nanowires using Nano X-ray Diffraction

Susanna Hammarberg

LUND
UNIVERSITY

DOCTORAL DISSERTATION

Doctoral dissertation for the degree of Doctor of Philosophy (PhD) at the Faculty of Science at Lund University to be publicly defended on the 2nd of June 2023 at 09.15 in Rydberg lecture hall, Department of Physics

Faculty opponent
Thomas Cornelius, Université de Toulon, Marseille, France

Organization LUND UNIVERSITY Division of Synchrotron Radiation Research Department of Physics, Box 118 S-221 00 Lund	**Document name** Doctoral thesis **Date of issue** 2023-06-02
Author Susanna Hammarberg	Sponsoring organization

Title and subtitle Strain Mapping of Single Nanowires using Nano X-ray Diffraction

Abstract

Nanowires are explored as basic components for a large range of electronic devices. The nanowire format offers several benefits, including reduced material consumption and increased potential for combining materials to form new novel heterostructures. Several factors, such as mechanical stress from contacting or a lattice mismatch in a heterostructure, can strain and change the lattice tilt. The strain is often intertwined with small gradients of composition. The strain relaxation can differ significantly from bulk due to the small diameters, but the mechanisms are not fully comprehended. X-rays have a penetrating power that makes it possible to investigate embedded samples without preparation or slicing. The high flux of coherent X-ray beams from synchrotron radiation facilities, combined with the nano-focus capabilities developed in recent years, have made it possible to probe nano-crystals. The 4th generation of synchrotrons, including MAX IV in Lund, Sweden, has even higher brilliance than previous sources. Diffraction imaging techniques using synchrotron radiation can reveal small strains down to 10^{-4}-10^{-5}. The field of coherent imaging pushes the limits of resolutions below the size of the focus. With Bragg ptychography, the displacement field in a crystal can be probed with resolution beyond the probe focus by numerically reconstructing the phase.

This thesis includes the development of X-ray nano-diffraction methods for the characterizing of nanowires, including GaInP/InP barcode nanowires, p-i-n InP nanowire devices and metal halide perovskite $CsPbBr_3$ nanowires. It includes a theoretical background of the scattering mechanisms in Thomson scattering in nano-crystals, goes through the formalism for coherent diffraction imaging, crystal structure and deformation in nanoobjects and the technical aspects of the experimental setup and measurement. Moreover, theoretical modelling of elastic strain relaxation in these nanowires was performed with finite element modelling.

Single III-V nanowire heterostructures and III-V nanowire devices were probed with scanning XRD and Bragg projection ptychography (BPP). How the techniques compare to each other and how the results are affected by the different approximations that are made in the respective technique was explored. Finite element simulations combined with nano-diffraction revealed that the lattice mismatch of 1.5% could be relaxed elastically for the diameter of 180 nm. From the strain mapping of the nanowire device, we found how the contacting of the nanowire bends the nanowire resulting in a tilt normal to the substrate.

Single perovskite metal-halide perovskite $CsPb(Br_{(1-x)}Cl_x)_3$ nanowire heterostructures were characterized with scanning nano-XRD and XRF, which showed that the lattice spacing was affected by composition and strain. Composition gradients revealed that Cl diffusion had taken place within the heterostructure. Furthermore, extracting the lattice tilts from shifts of the Bragg peak revealed a ferroelastic domain structure with simultaneously existing lattice tilts. These findings are beneficial for the further development of MHP nanowires devices.

Key words
X-ray diffraction, III-V semiconductors, perovskites, MHP, nanowires, heterostructures, XRF

Classification system and/or index terms (if any)

Supplementary bibliographical information		**Language** English
ISSN and key title		**ISBN** 978-91-8039-653-0 (print) 978-91-8039-654-7 (electronic)
Recipient's notes	**Number of pages 68**	Price
	Security classification	

Signature Date 2023-04-14

Strain Mapping of Single Nanowires using Nano X-ray Diffraction

Susanna Hammarberg

LUND
UNIVERSITY

Cover image: Simulated nano-diffraction Bragg peak image extended with AI generator DALL·E.

Division of Synchrotron Radiation Research
Department of Physics, Faculty of Science
Lund University
SE-221 00, Lund
Sweden

ISBN 978-91-8039-653-0 (print)
ISSN 978-91-8039-654-7 (electronic)

Printed in Sweden by Media-Tryck, Lund University
Lund 2023

Table of Contents

List of publications

This thesis is based on the following publications, referred to by their Roman numerals:

I. *High resolution strain mapping of a single axially heterostructured nanowire using scanning X-ray diffraction*

Hammarberg, S., Dagytė, V., Chayanun, L., Hill, M.O., Wyke, A., Björling, A., Johansson, U., Kalbfleisch, S., Heurlin, M., Lauhon, L.J., Borgström, M.T. and Wallentin, J.

Nano Research, *13*(9): p. 2460-2468. (2020)

DOI: 10.1007/s12274-020-2878-6

I measured and analysed the data from MAX IV, performed the analysis and the simulations, prepared the figures, and wrote the manuscript.

II. *Fast nanoscale imaging of strain in a multi-segment heterostructured nanowire with 2D Bragg ptychography*

Hammarberg, S., Dzhigaev, D., Marçal, L. A. B., Dagytė, V., Björling, A., Borgström, M. T., Wallentin, J.

Manuscript (under review)

I measured and analysed the data from MAX IV, performed the data analysis and the simulations, prepared the figures, and wrote the manuscript.

III. *Nanofocused scanning X-ray diffraction of single heterostructured $CsPbBr_3$ - $CsPb(Br_{(1-x)}Cl_x)_3$ perovskite nanowires*

Hammarberg, S., Marçal, L. A. B., Björling, A., Wallentin, J.

Manuscript

I took part in the experiment at MAX IV, performed the data analysis, prepared the figures, and wrote the manuscript.

IV. *Combining nanofocused X-rays with electrical measurements at the NanoMAX beamline*

Chayanun, L., Hammarberg, S., Dierks, H., Otnes, G., Björling, A., Borgström, M.T. and Wallentin, J.

Crystals, *9*(8): p.432. (2019)

DOI: 10.3390/cryst9080432

I participated in the experiment at MAX IV, did the data analysis for the diffraction data, prepared a figure, and took part in editing of the manuscript.

Publications not included in this thesis, to which I have contributed during my Ph.D:

Inducing ferroelastic domains in single-crystal $CsPbBr_3$ perovskite nanowires using atomic force microscopy

Marçal, L.A.B., Benter, S., Irish, A., Dzhigaev, D., Oksenberg, E., Rothman, A., Sanders, E., Hammarberg, S., Zhang, Z., Sala, S. and Björling, A., Unger, E., Mikkelsen, A., Joselevich, E. Timm, R., and Wallentin, J.

Physical Review Materials, *5*(6): p L063001. (2021)

DOI: 10.1103/PhysRevMaterials.5.L063001

In situ imaging of ferroelastic domain dynamics in $CsPbBr_3$ perovskite nanowires by nanofocused scanning X-ray diffraction

Marçal, L.A.B., Oksenberg, E., Dzhigaev, D., Hammarberg, S., Rothman, A., Björling, A., Unger, E., Mikkelsen, A., Joselevich, E. and Wallentin, J.

Acs Nano, *14*(11): p.15973-15982. (2020)

DOI: 10.1021/acsnano.0c07426

Strain mapping inside an individual processed vertical nanowire transistor using scanning X-ray nanodiffraction

Dzhigaev, D., Svensson, J., Krishnaraja, A., Zhu, Z., Ren, Z., Liu, Y., Kalbfleisch, S., Björling, A., Lenrick, F., Balogh, Z.I. and Hammarberg, S., Wallentin, J., Timm, R., Wernersson, LE. and Mikkelsen, A.

Nanoscale, *12*(27): pp.14487-14493. (2020)

DOI: 10.1039/D0NR02260H

Coherent Bragg imaging of 60 nm Au nanoparticles under electrochemical control at the NanoMAX beamline

Björling, A., Carbone, D., Sarabia, F.J., Hammarberg, S., Feliu, J.M. and Solla-Gullón, J.

Journal of synchrotron radiation, *26*(5): p.1830-1834. (2019)

DOI: 10.1107/S1600577519010385

Nanoscale mapping of carrier collection in single nanowire solar cells using X-ray beam induced current

Chayanun, L., Otnes, G., Troian, A., Hammarberg, S., Salomon, D., Borgström, M.T. and Wallentin, J.

Journal of synchrotron radiation, *26*(1): p.102-108. (2019)

DOI: 10.1107/s1600577518015229

Nanobeam X-ray fluorescence dopant mapping reveals dynamics of in situ Zn-doping in nanowires

Troian, A., Otnes, G., Zeng, X., Chayanun, L., Dagyte, V., Hammarberg, S., Salomon, D., Timm, R., Mikkelsen, A., Borgström, M.T. and Wallentin, J.

Nano letters, *18*(10): p. 6461-6468. (2018)

DOI: 10.1021/acs.nanolett.8b02957

List of abbreviations

2D	Two-dimensional
3D	Three-dimensional
AAO	Anodized aluminium oxide
BCDI	Bragg coherent diffractive imaging
BPP	Bragg projection ptychography
CDI	Coherent diffractive imaging
DM	Difference map
DLSR	Diffraction-limited storage ring
ER	Error reduction
ePIE	extended ptychographic iterative engine
FEM	Finite element modelling
FOV	Field of view
FFT	Fast Fourier transform
HIO	Hybrid input output
KB	Kirkpatrick-Baez
LINAC	Linear accelerator
LED	Light-emitting diode
maBPP	Multi-angle Bragg projection ptychography
MHP	Metal halide perovskite
PIE	Ptychographic iterative engine
PL	Photoluminescence
SEM	Scanning electron microscopy
SSA	Secondary source aperture
STEM	Scanning transmission electron microscopy
STXM	Scanning transmission X-ray microscopy
TEM	Transmission electron microscopy
XBIC	X-ray beam induced current
XRD	X-ray diffraction
XRF	X-ray fluorescence

Popular scientific summary

X-rays are known to the public as a tool to see bones and teeth at the hospital and dentist, but there are many more, less commonly known, uses of X-rays. Just as X-rays can penetrate tissue to reveal the bones within, they can pass through other materials. For example, X-rays can penetrate the visible layer of a Rembrandt painting to reveal what was painted underneath. Synchrotron radiation X-rays are the same as the radiation used in medical imaging, but possess distinct properties that make them a more powerful tool for a wide range of scientific applications. Most importantly, synchrotron X-ray beams can be generated at a much higher intensity and smaller spot sizes, enabling the detection of signals from objects as small as nanometers (0.000000001 m). It is a valuable tool in the field of material and life sciences to precisely map the composition and structure of various materials, such as biological samples and ores from the earth, among many other applications. MAX IV in Lund, Sweden, is a synchrotron radiation facility inaugurated in 2016. This thesis concerns the mapping of physical properties in nano-objects using synchrotron radiation, with a particular class of experiments that involve X-ray diffraction. One of the experiments was performed at MAX IV as one of the first of its kind in 2017. In the following years, several more experiments followed, with more advanced methods and varying materials, but commonly involving *nanowires*.

Nanowires are small cylinders with diameters on the nanometer scale that can be used to produce transistors, light-emitting diodes and solar cells. Fabricating devices in the nanowire format has a lot of advantages. The amount of material used is greatly reduced, which lowers the costs. Materials that cannot be combined in bulk format can be combined in the nanowire format. A lot of physics, for example, how electric current runs through an object, is different when the dimensions of the objects are within this very small regime, which can be utilised to, for example, produce more energy-efficient solar cells. This requires that we can measure these qualities with high accuracy and resolution. These issues are addressed in this thesis, were we developed the methodology to measure the composition and structure of nanowires and nanowire devices with X-ray diffraction using synchrotron radiation.

A semiconductor has electrical conductivity lower than a conductor but higher than an insulator. It is used in electrical components such as diodes and transistors to control and manipulate electrical signals. III-V semiconductors are a class of semiconductors which are used for solar cells and light emitting diodes. We have characterized III-V nanowires grown at Lund University. In addition, we have investigated nanowires made from metal halide perovskites, a new class of materials with significant potential in the photovoltaics industry. A new type of metal halide perovskite nanowire is investigated in this thesis, where we probed the composition and structure. In summary, the implementation of advanced synchrotron X-ray

characterizing techniques for nanowires in this thesis paves the way for the development of new, more efficient devices.

Populärvetenskaplig sammanfattning

Röntgenstrålning är känt för allmänheten som ett verktyg att se ben och tänder på sjukhus, men det finns många fler mindre kända användningsområden. Precis som röntgenstrålning tränger igenom vävnad för att exponera benen inuti, så kan den tränga igenom andra material. Till exempel kan röntgenstrålning användas för att se igenom det yttersta lagret färg på en Rembrandt-målning och avslöja att det finns en tidigare målning under som målades över. Röntgenstrålning från en synkrotron är lik den som används för medicinsk avbildning men med distinkta egenskaper som gör det till ett kraftfullare verktyg för ett brett spektrum av vetenskapliga tillämningar. En synkrotronljuskälla kan generera en röntgenstråle med mycket hög intensitet och liten fokusstorlek, vilket gör det möjligt att detektera signaler från objekt så små som några nanometer (0.000000001 m). Det är ett värdefullt verktyg för att kartlägga sammansättningen och strukturen hos olika material inom material- och livsvetenskaper så som biologiska prover, proteiner, jordmalmer eller metaller. MAX IV i Lund, Sverige, är en synkrotronljusanläggning som invigdes 2016. Denna avhandling handlar om kartläggning av fysiska egenskaper i nano-objekt med hjälp av synkrotronljus med en särskild klass av experiment som innefattar röntgendiffraktion. Ett av experimenten utfördes vid MAX IV som ett av de första i sitt slag 2017. Under de efterföljande åren följde många fler experiment med mer avancerade metoder och varierande material, men gemensamt för alla var att proven var *nanotrådar*.

Nanotrådar är små cylindrar med diametrar på nanometerskalan som kan användas för att producera till exempel transistorer, ljusdioder eller solceller. Att tillverka komponenter i formatet av nanotrådar har många fördelar. Den mest uppenbara är att mängden material som används minskar kraftigt, vilket sänker kostnaderna. Dessutom kan material som inte kan kombineras i större format faktiskt fungera att kombinera i en nanotråd. Mycket av fysiken, till exempel hur ström går genom materialet, är annorlunda när dimensionerna hos objekten är så små, vilket kan förändra komponenternas egenskaper. Detta kan utnyttjas för att, till exempel, producera mer energieffektiva solceller, men det förutsätter att vi kan mäta egenskaperna med stor noggrannhet. Detta ämne adresseras i denna avhandling, där vi har utvecklat metoder för att mäta sammansättningen och strukturen hos nanotrådar och nanotråds-komponenter med röntgendiffraktion från en synkrotron.

En halvledare leder elektroner bättre än en isolator men sämre än en ledare. III-V material är en klass av halvledare som används i solceller och lysdioder. Vi har karaktäriserat III-V nanotrådar som tillverkats vid Lunds universitet. Vi har också undersökt nanotrådar gjorda av ett nyligen upptäckt material, metallhalidperovskiter, med hög potential inom solcellsindustrin. En ny typ av nanotrådar i metallhalidperovskit har tillverkats i vår grupp, och vi har undersökt struktur och sammansättning med röntgendiffraktion. Sammanfattningsvis banar

metoder för högupplösta karaktärisering av nanotrådar med synkrotronljus vägen för utvecklingen av nya, mer effektiva komponenter.

Acknowledgements

Before embarking on the topics of this thesis, I want to express my gratitude to the ones who made it all possible.

First and foremost, I want to thank my principal supervisor Jesper Wallentin, for all the fun and all support over the past few years. I appreciate your dedication to my development as a researcher and to the success of my projects. You have consistently made time to help me promptly, even when you have had busy times. Thank you for the opportunity to take on a PhD in your group with all the experiences, including travels, conferences, and beamtimes, that it brought, I am grateful.

I want to thank my co-supervisors: Anders Mikkelsen, for your positive attitude to research and for involving me in new projects, and Alexander Björling, for the hands-on help with the numerical side of imaging and for your encouragement.

Thanks to the team at NanoMAX for an eminent place to do experiments. Beyond the excellent experimental conditions and beamline support, I have always found a nice atmosphere there.

To the people who collaborated with me on beamtimes: Dmitry Dzhigaev, Lert Chayanun, Andrea Troian, Huaiyu Chen, Hanna Dierks, and Megan Hill, thank you. Megan, I am thrilled that our paths crossed during your project here. Thanks to Robin Svärd for knowing so much about accelerators when I had bananas. Thanks to Lucas Marcal, Zhaojun Zhang and Nils Lamers for supporting me when embarking onto the field of perovskites, and to Zhaojun, Nils and Dagyte Vilgaile for providing me with samples.

I could not have asked for a better and friendlier division to do my PhD than sljus, where I enjoyed meeting people from all over the world in the lunchroom; lucky me! Especially thanks to: Giulio, who made it fun to go into the office every morning, Hanna for proofreading, units, art, overall support and for all the good times outside the department, Bart whose positive attitude was contagious, Dima who is the boss of coherent diffraction and the best resource to have close by, Virgi who is cool and kind (so cool, she does not care what people say about her office chair), David who has a brain and heart larger than a bee's and to Yen-Po who leaves everyone he meets in a happier and calmer state. Thanks to Sandra, Emma, Andrea, Lucas W, Lucas M and everyone else with whom I shared good times at sljus. Thanks to Patrik and Anne for all the administrative help and to Patrik for all discussions; it has been a pleasure disagreeing with you.

Lastly, I want to thank my family for always having my back and for all the good times that we share. Thank you Tommy and Ammi for being so thoughtful and caring. To my friends Hanna, Sanna, Amanda, David, Lena, Emma, Ida, Julia, Fredrik, Martha and Erik, thanks for all the laughs and escapades. To Lone, my little

energy package, I love you, and to life's best pizza with perfect topping that is my Johannes, I love you.

Thank you!

1 Introduction

This thesis concerns the characterization of nanowires using X-ray diffraction imaging and the development of these methodologies. Nanowires are one-dimensional crystal rods with a significantly longer length than diameter. External or internal stresses on a nanowire can strain its crystal and make it deviate from its ideal state. The strain can have a significant impact, positive or negative, on the properties and behaviour of nanowire-based devices. The dimensions of nanowires, and the relevant strain sensitivities, require state-of-the-art imaging methods.

MAX IV laboratory, see Figure 1.1 (a), produces X-ray beams with outstanding quality, making the facility a powerful resource for materials and life sciences. It is situated in Lund, Sweden and was commissioned and opened up for experiments at several beamlines in 2017. The results in this thesis are partially based on one of the very first experiments for users at the NanoMAX beamline and the first nano-XRD diffraction imaging experiment. This beamline focuses on techniques that utilise MAX IV's capacities to the fullest.

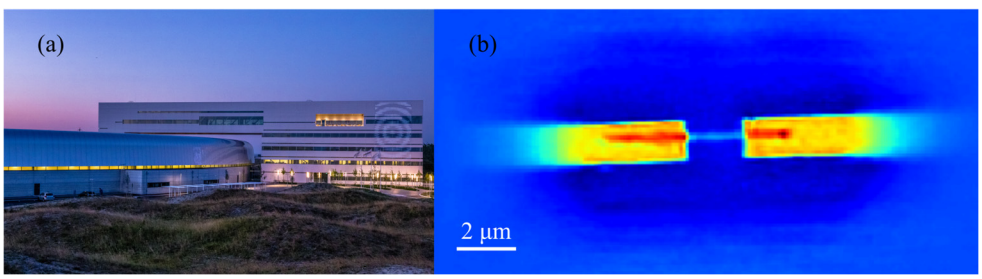

Figure 1.1 (a) A photo of MAX IV Laboratory. Photo credit www.maxiv.lu.se. (b) High resolution phase image of a contacted nanowire from X-ray ptychography.

Several techniques exist for imaging objects with sub-micron sizes. Transmission electron microscopy (TEM) can be used to characterize nanostructures with atomic resolution [1] but requires thin samples or sample slicing that can alter the structure in itself. X-rays have the advantage over electron probes that they can penetrate longer into matter and probe embedded objects. Another major advantage is the outstanding strain sensitivity, which is usually in the range 10^{-4} to 10^{-5}. In recent times, developments in X-ray optics have opened up the opportunity to focus hard X-rays to the nanoscale [2, 3]. For example, at the NanoMAX beamline, the X-ray

beam can be focused to below 50 nm. To characterize a very thin sample, like a nanowire, the nanofocus is meaningless if the number of photons is insufficient for a measurable signal. MAX IV can generate X-ray beams with a high number of photons in a small spot size. Another advantage of a synchrotron source, compared to a lab source, is that the X-ray energy can be tuned over a wide range.

Scanning X-ray diffraction (XRD) is sensitive to shifts in crystal lattices and can be used to map variations in nanoscale objects, including strain, composition and crystal structure, using a nanofocused X-ray beam. Coherent diffraction imaging (CDI) methods have recently emerged as a field of techniques with great potential for strain imaging, as it is highly sensitive to strain in crystals and has sub-beam resolution capabilities. These include the technique ptychography, see example in Figure. 1.1 (b). Here, the resolution is no longer limited by the X-ray nanofocus, but requires a fully coherent beam throughout the sample.

This thesis' major materials system is nanowires based on III-V semiconductors, a group of materials used in many types of modern electronic and optoelectronic devices, and further ventures into the emerging field of metal halide perovskite (MHP) nanowires. III-V semiconductors are expensive, but in the nanowire geometry, the material consumption can be reduced potentially up to 90% with retained efficiency [4, 5]. Heterostructures can be formed more easily without defects [6] in nanowires due to radial strain relaxation. In this way, the electronic band structure can be tailored to suit the needs of the applications.

Strain in nanowires can affect electrical and thermal conductivity, mechanical endurance, and the bandgap, emphasizing the importance of mapping the strain distribution. With precise knowledge about the strain and other changes in the crystal structure, materials can be controlled and manipulated to improve performance in practical applications. How the strain is distributed in nanowires compared to bulk materials is not thoroughly understood, especially since larger lattice mismatches can be accommodated. This thesis aims at improving the methods for producing nanowire strain maps using X-rays from a synchrotron radiation source. X-rays also probe other types of variations in the crystal, including composition and crystal structure. We use finite element modelling (FEM) and X-ray fluorescence mapping to help separate these components and develop a FEM-based model for the nano-diffraction experiments.

The outline of the thesis is as follows:

The thesis starts with the theory of the underlying mechanisms in X-ray diffraction of crystals and a derivation of the equations used in the analysis in **chapter 2**. In **chapter 3** follows a general introduction to synchrotron radiation and the focusing techniques at coherent imaging beamlines, as well as a specific introduction to the synchrotron and beamline used in this thesis, MAX IV laboratory and the NanoMAX beamline. Equipped with that background, the reader is introduced more specifically to the methods and results of this thesis. First, **chapter 4** explains the

experimental techniques used and our specific implementation for nanowires. **Chapter 5** summarizes the findings in the papers; how the strain and tilts were distributed for the different types of strain origins. The thesis ends with **chapter 6** and a summary and outlook of the subject.

2 X-ray diffraction from crystals

In this chapter, X-rays interact with a nanocrystal, propagate, and produce diffraction patterns revealing the inner structure of the nanocrystal.

2.1 The nature of X-rays

Throughout this thesis, X-ray beams are the main probes. The reason is that they are highly penetrable and also highly sensitive to variations in nanocrystals' structure. Wilhelm C. Röntgen was the first to report on the invisible radiation that he called 'X-rays' in 1895. It was later concluded that X-rays are electromagnetic radiation with energies between 100 eV and about 100 keV, found between UV light and gamma rays in the electromagnetic spectrum. In the 1900s, quantum mechanics introduced wave-particle duality, which explains that electromagnetic radiation, like X-rays, can exhibit both wave and particle behaviour. In the particle picture, the quantization of light is referred to as photons. The relation between the energy of a photon and its wavelength is:

$$E = hc/\lambda, \tag{2.1}$$

where h is Planks constant and c is the speed of light in vacuum. X-rays have a wavelength in the range of about 10 nm to 0.1 Å, where the unit Ångström is equal to 1 Å = 10^{-10} m, corresponding to energies of around 0.1 to 100 keV.

As Röntgen experimented with his newfound rays, he saw that they could easily pass through paper, cardboard, and when placing his hand in the X-ray path, he even saw that the rays had penetrated his flesh, which created an image of his bones on the other side [7]. The contrast was formed from the primary way that X-rays interact with matter, *photoelectric absorption*. As it is very element sensitive, a contrast was formed between bones and tissue. Although this is the primary way to create a contrast in X-ray physics, there are other ways. This thesis makes use of scattering as a contrast mechanism, and therefore the theory of the scattering mechanisms will take up most of the upcoming chapter.

2.2 X-ray interaction with matter

X-rays in matter interact with the atomic electrons, while interaction with the atomic nuclei or its constituents has a low probability. As an example, the ways X-ray matter interacts with carbon are displayed in Figure 2.1. The most probable interaction for X-rays is photoelectric *absorption*. Here, X-rays are absorbed by a core electron in the atom that is emitted from the atom leaving a vacancy. An electron from a higher energy level is deexcited to fill the vacancy. The excess energy from that electron is released as a photon or transferred to an electron in a higher energy shell, an Auger electron, which is ejected from the atom. If the excess energy is released by a photon, it is known as *X-ray fluorescence* (XRF).

The cross-section for X-ray absorption is very material-dependent, approximately scaling with the atomic number as Z^4 [8]. As it depends on the energy of the atomic binding energies, it is also very energy dependent, see Figure 2.1 for an example in carbon. The X-ray energy region is marked with dashed red lines. The absorption cross-section decreases with X-ray energy but has peaks called *absorption edges* where the photon energy matches a new binding energy of a core atom.

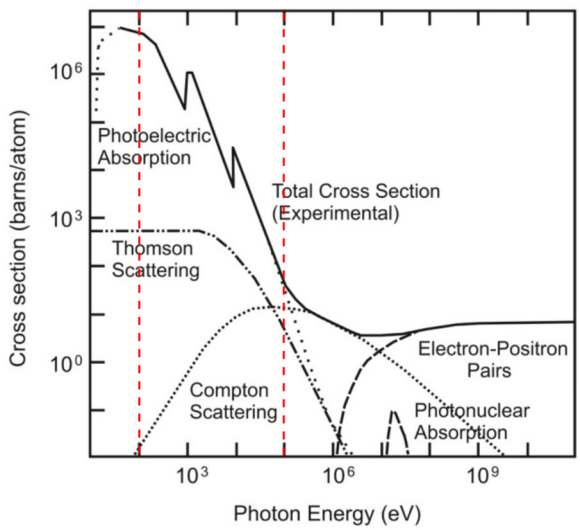

Figure 2.1 The total cross-sections for photon interaction with carbon expressed as barns/atom, together with its constituent types of interaction, as a function of photon energy. The approximate energy range of X-rays is indicated on the graph by red dashed lines. This thesis concerns X-rays with an energy on the order of 10^4 eV. Figure from Ref. [9], where it was adapted from Ref. [10].

X-ray fluorescence has been used to some extent in all experiments in this thesis. Compared to X-ray diffraction, it is easy to measure as it gives a signal in any direction. Therefore, it has been used to localise single nanowires in the experimental setup, as well as for elemental mapping. A fluorescence photon will

have the same energy as the energy difference between the two energy levels in the originating atom. All elements illuminated by the incident beam can generate peaks in the XRF spectra, if it has a binding energy below the energy of the beam.

The secondary process of interaction is *scattering*, when the incoming photon interacts with an electron without getting absorbed. In Figure 2.1, this process is divided into *Thomson scattering* and *Compton scattering*. In Thomson scattering, the photon interacts with an electron in an *elastic* process, meaning that the interaction does not change the energy of the photon. In contrast, Compton scattering is *inelastic*, where the photon transfers some of its energy to the electron as recoil energy. Diffraction patterns are formed from constructive interference from coherent scattering, that is, photons that scatter with the same energy and phase. This is the case for Thomson, but not Compton scattering. As such, Thomson scattering is the process that produces the images in this thesis and is discussed in greater detail in the following section.

2.2.1 Thomson scattering

We will start by describing Thomson scattering as a single scattering event involving a single electron and then gradually build up the theory to cover elastic scattering of a nanocrystal.

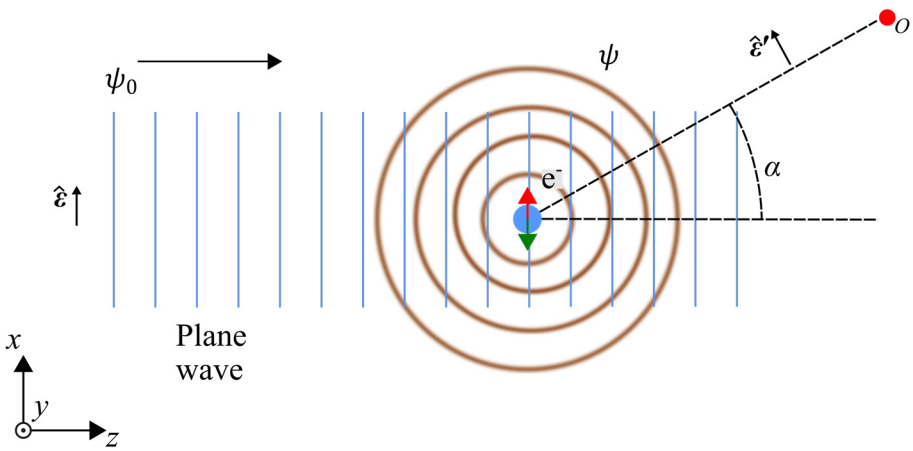

Figure 2.2 Illustration of Thomson scattering of X-rays on a single free electron. A monochromatic linearly polarized incident X-ray beam approximated as plane waves propagates along *z* and scatters off an electron illustrated with a blue circle. The electric field of the X-rays sets the electron in an oscillatory movement in the same direction, that is, along *x*. The oscillating electron acts as a dipole and emits spherical waves. Note that the drawn lines are wavefronts, not the amplitude of the scattered wave. The amplitude of the scattered wave is not uniform, as explained in the text. $\hat{\varepsilon}$ and $\hat{\varepsilon}'$ denote the unit vectors of the electric field of the incident and scattered wave, respectively.

A single electron X-ray scattering event is depicted in Figure 2.2, and here we will start with a description based on classical physics. A linearly polarized X-ray field ψ_0, is propagating along z polarized with the electric field $\boldsymbol{E}(\boldsymbol{r})$ in the direction x. The electric field sets the electron in an oscillatory movement along x, perpendicular to the direction of propagation z. The force exerted on the electron is: $\boldsymbol{F} = -e\boldsymbol{E}(r)$, and the electron is accelerated according to:

$$\boldsymbol{a}_T = -\frac{e\boldsymbol{E}(\boldsymbol{r})}{m}, \tag{2.2}$$

where the direction of $\boldsymbol{a}_T$ is the same as $\boldsymbol{E}(\boldsymbol{r})$. The electron is an electric charge, accelerated in an electric field, and as such, it is a dipole that emits radiation in the form of spherical waves. The strength of the emitted wave will depend on the incident wave's electric field. The radiated field at an observation point at angle α in the xz-plane is [8]:

$$\psi(\boldsymbol{r}) = -r_0\psi_0\frac{e^{i\boldsymbol{k}\boldsymbol{r}}}{\boldsymbol{r}}\cos(\alpha). \tag{2.3}$$

Since the electron has a negative charge, the direction of the accelerated motion is opposite to the direction of the electric field of the incident radiation. In other words, the radiated field from Thomson scattering has a phase shift of 180° compared to the incident field [11], as illustrated in Figure 2.2.

The radiated intensity from a dipole is not uniform in all directions, and the modified amplitude is included in the term $\cos(\alpha)$. In Figure 2.2, the acceleration is along the x-axis, so at an observation point along the x-axis, at $\alpha = 90°$, the radiated intensity is zero, while at $\alpha = 0°$ it is at maximum. The factor $\cos(\alpha)$ in Eq. (2.3) originates from the scalar product between the polarization unit vectors of the incident $\hat{\boldsymbol{\varepsilon}}$ and emitted field $\hat{\boldsymbol{\varepsilon}}'$.

The pre-factor r_0 in Eq. (2.3), is the *Thomson scattering length*, or *classical electron radius*. The *scattering amplitude* for Thomson scattering of a single electron is [8]:

$$A(\alpha) = -r_0|\boldsymbol{\varepsilon}\boldsymbol{\varepsilon}'|. \tag{2.4}$$

We know from modern physics that the electron is not a particle with a specific size, however, r_0 is the relevant length scale for calculating cross-sections of scattering, and a quantum mechanical description gives the equivalent result for scattering amplitude [8]. As seen in Eq. (2.4), the scattering amplitude is independent of the incident photon energy for free electrons. In the X-ray energy range, the photons have enough energy for the electrons to respond to a good approximation as if they were free [8].

In the quantum mechanical description of Thomson scattering, the X-rays consist of photons with energies quantized by hc/λ. These are absorbed by the electron, leaving the electron in an excited state. To de-excite to the ground state, the electron releases a photon with the same energy as the incoming photon.

From what we now know about X-ray interaction with matter, we can revisit the claim about what constituents in matter scatter X-rays. Since the mass of the proton is about 2000 times larger than the electron, the acceleration of the proton is much weaker. Neutrons, as uncharged particles, stay unaffected by X-rays.

2.2.2 Kinematical scattering from multiple scatterers

Up to now, we have discussed Thomson scattering of a single free electron. Now we want to expand the discussion to X-ray elastic scattering from a solid. As previously discussed, the electrons in the solid will be considered free. The scattered wavefield then consists of the summed contribution of every single free electron scattering event.

To continue the description, an important approximation will come into play, the *Born* approximation. This requires that scattering is fairly weak so that a photon scatters only once while secondary scattering is neglected [12]. Scattering under this approximation is known as *kinematical scattering*, see Figure 2.3.

Throughout this thesis, kinematical scattering will be assumed and will be measured far away from the samples. As depicted in Figure 2.3, all Thompson scattering events give rise to a spherical wave creating a set of interfering spherical waves. As these propagate, the wavefronts are considered first as interfering parabolic waves, but at a distance far away from the scatterers, as plane waves. This imaging regime is the *Fraunhofer* or *far field regime*. For a plane wave of wavelength λ, incident upon a sample that has features on the length scale a_s, this regime occurs at a distance R conditioned by:

$$R \gg \frac{a_s^2}{\lambda}. \tag{2.5}$$

The largest feature to be considered should be used for a_s, since a large feature, with further separated points, requires a longer distance to diffract [12].

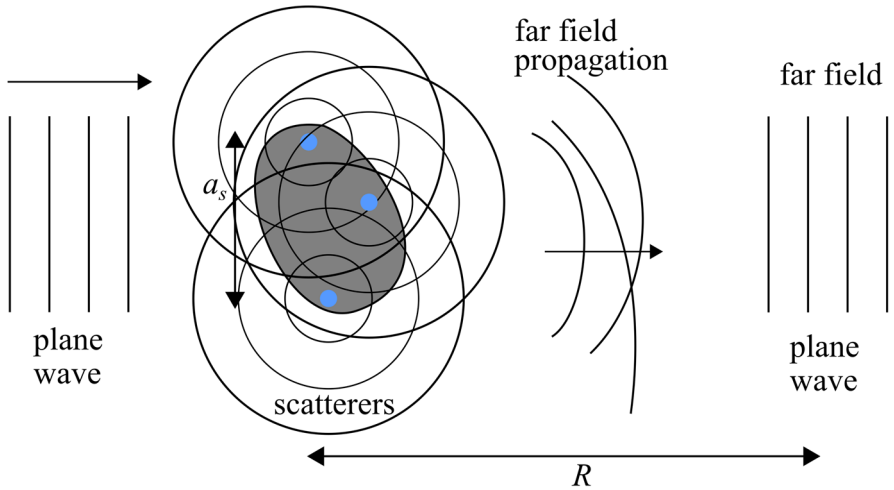

Figure 2.3 Far field diffraction of X-rays. A monochromatic X-ray field is approximated as a plane wave designated by the vertical lines incident from the left. Each scattering event gives rise to a spherically propagating wave. In the far field, the wave field can be approximated as a plane wave.

In the following, we consider Thomson scattering events from two volume elements in a solid, see Figure 2.4. Here, $\boldsymbol{k}_i$ and $\boldsymbol{k}_f$ represents the incoming and outgoing wave vectors, respectively. It is convenient to define a *scattering vector* $\boldsymbol{q}$ to describe the scattering:

$$\boldsymbol{q} = \boldsymbol{k}_f - \boldsymbol{k}_i. \tag{2.6}$$

In elastic scattering, the wavelength does not change, so the magnitude of the incoming and the outgoing wave is the same $|\boldsymbol{k}_f| = |\boldsymbol{k}_i|$.

Looking at the geometry in Figure 2.4, we want to find an expression for the X-rays after scattering from two electrons separated with $\boldsymbol{r}$. The interference is evaluated at an observation point in the far field where the scattered waves can be approximated as plane waves, which means that their $\boldsymbol{k}$-vectors are parallel. The X-ray that scatters at $O + \boldsymbol{r}$ has travelled an extra path of $\sin(\alpha)|\boldsymbol{r}|$ compared to the one scattered at O. Translated to phase, the phase shift $\Delta\phi$ between the X-rays is:

$$\Delta\phi = \frac{2\pi\sin(\alpha)|\boldsymbol{r}|}{\lambda} = |\boldsymbol{k}_i||\boldsymbol{r}|\cos(90 - \alpha), \tag{2.7}$$

which is the scalar product $\boldsymbol{k_i r}$.

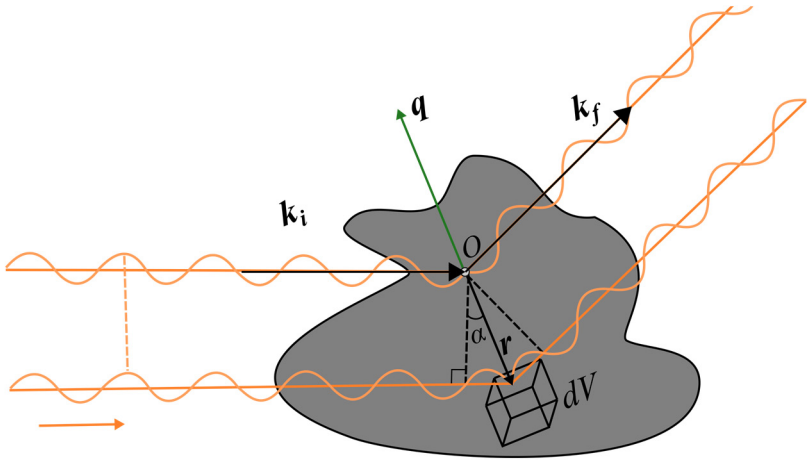

Figure 2.4 Thomson scattering from a solid. One X-ray scatters off a volume element *dV*, and a second X-ray scatters off a point *O* separated from the volume element with a vector ***r***.

In the same manner, the phase shift after scattering gives a phase shift of $-\boldsymbol{k}_f\boldsymbol{r}$ and is added to the scattering from the second wave so that the total phase shift is:

$$\Delta\phi = (\boldsymbol{k}_i - \boldsymbol{k}_f)\boldsymbol{r} = -\boldsymbol{q}\boldsymbol{r}. \qquad (2.8)$$

A phase factor of $e^{-i\boldsymbol{q}\boldsymbol{r}}$ is added to the scattered amplitude for every scattering event. To generalise to the scattering of all electrons in a volume, the electrons can be modelled with the concept of the electron density $\rho(\boldsymbol{r})$, which is the number of electrons per unit of volume. The integral of $\rho(\boldsymbol{r})$ over all volume elements results in the number of electrons in the sample, and $\boldsymbol{r}$ is the positional vector for each scatterer. Under the kinematical approximation the elastic scattering amplitude in the far field in the direction $\boldsymbol{k}_f$ will be proportional to the sum of scattering from all volume elements, and the phase shift factor is added to each element. The strength of each scattering event is r_0 and it follows that the scattering amplitude from all volume elements becomes:

$$A(\boldsymbol{q}) = r_0 \int \rho(\boldsymbol{r}) e^{-i\boldsymbol{q}\boldsymbol{r}}\, d\boldsymbol{r}. \qquad (2.9)$$

If the electron density includes all electrons in a single atom, $A(\boldsymbol{q})/r_0$ is the *atomic form factor* $f(\boldsymbol{q})$. Eq. (2.9) is, by definition, the Fourier transform of the electron density $\rho(\boldsymbol{r})$. It can be concluded that the relationship to the far field is a transformation between real space and reciprocal space. As a consequence, a broad electron density in real space will give a narrow intensity in reciprocal space and vice versa.

The electrons in an atom are of course not free but bound to the nucleus. The corrections to the atomic form factor to account for this are known as the *dispersion corrections*. For photon energies larger than the K-shell binding energy, the dispersions corrections are negligible. The corrections become especially relevant at X-ray energies close to an absorption resonance where absorption is more likely.

2.3 Diffraction from a crystal

2.3.1 Crystal structure

When the atoms in a solid are arranged in a disordered manner, as in glass, it is called amorphous. However, a large fraction of materials are crystalline, with atoms arranged on a regular grid, referred to as the *crystal lattice*. The spacing in a crystal lattice is in the order of a few Ångström (0.1 nm). When the same crystal lattice is repeated throughout the material without interruptions, it is a single crystal, but it can also be built up by grains; areas of different sizes where the lattice is in another orientation.

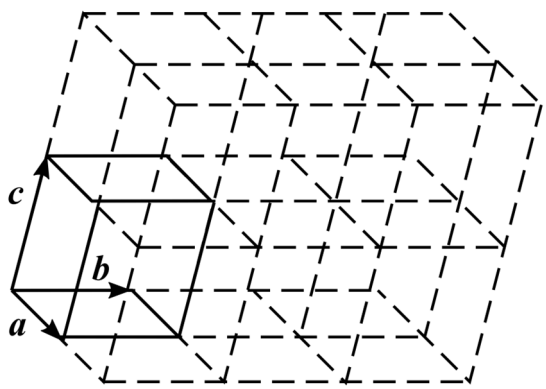

Figure 2.5 An ideal crystal lattice with basis vectors.

A crystal can be seen as made up of building blocks that are stacked in 3D, and the smallest building block that can be constructed is the *unit cell.* There is a conventional classification system for these cells, which can be e.g., cubic or orthorhombic. To define the cells, three basis vectors $(\boldsymbol{a}, \boldsymbol{b}, \boldsymbol{c})$ are defined, see Figure 2.5. In the cubic system, the sides have equal length, $|\boldsymbol{a}| = |\boldsymbol{b}| = |\boldsymbol{c}| = a$. All points in the lattice vector can be reached by the lattice vector $\boldsymbol{R}_n$:

$$\boldsymbol{R}_n = \mathrm{n}_1\boldsymbol{a} + n_2\boldsymbol{b} + n_3\boldsymbol{c}, \tag{2.10}$$

where n_1, n_2, n_3 are integers.

A fundamental concept in crystal diffraction is the *reciprocal lattice*. We saw earlier that in kinematical scattering, the scattered wave in the far field is proportional to the Fourier transform of the electron density. If the sample plane consists of a lattice, the scattered wave will be the Fourier transform, which is another lattice. The construction of a reciprocal lattice facilitates the analysis of X-ray diffraction. The basis vectors in the reciprocal lattice are defined by:

$$\boldsymbol{a}^* = \frac{2\pi}{V}\boldsymbol{b} \times \boldsymbol{c}, \quad \boldsymbol{b}^* = \frac{2\pi}{V}\boldsymbol{c} \times \boldsymbol{a}, \quad \boldsymbol{c}^* = \frac{2\pi}{V}\boldsymbol{a} \times \boldsymbol{b}, \quad (2.11)$$

where V is the volume of the cell, given by: $V = \boldsymbol{a} \cdot (\boldsymbol{b} \times \boldsymbol{c})$. The spacing between two lattice points in the reciprocal lattice in the direction of $\boldsymbol{a}^*$ is not a, but $2\pi/a$.

The reciprocal lattice vector is defined by:

$$\boldsymbol{G}_{hkl} = \mathrm{h}\boldsymbol{a}^* + k\boldsymbol{b}^* + l\boldsymbol{c}^*, \quad (2.12)$$

where (h,k,l) are integers usually referred to as the *Miller indices*. The Miller indices are used to indicate planes in the crystal lattice, describing where the plane should cut the lattice axes. When indicating a plane, the Miller indices are within brackets (h,k,l). When indicating a set of planes it is denoted $\{h, k, l\}$ [13]. The spacing between the planes is called the *d-spacing*, denoted by d_{hkl} and related to the reciprocal lattice vector $\boldsymbol{G}_{hkl}$ with [14]:

$$d_{hkl} = \frac{2\pi}{|\boldsymbol{G}_{hkl}|}. \quad (2.13)$$

The scattering amplitude from each unit cell is related to the form factor of each atom j in the cell. The scattering amplitude from a unit cell is r_0 times the *structure factor* $F(\boldsymbol{q})$, this is the sum of the form factor of each atom $f_j(\boldsymbol{q})$, with an added phase factor for each atom according to:

$$F(\boldsymbol{q}) = \sum_{j=1}^{J} f_j(\boldsymbol{q}) e^{-i\boldsymbol{q}\boldsymbol{r}_j}. \quad (2.14)$$

The scattering amplitude for the whole crystal is discussed in the upcoming sections.

2.3.2 Bragg's law

Now we will turn our attention to the problem of Thomson scattering from a perfect crystal. In this geometrical argumentation on crystal diffraction, the term reflection will be used, which is the corresponding macroscopic phenomenon to elastic scattering [8]. Bragg's law illustrates why crystals diffract X-rays at discrete angles

and how they are proportional to the crystal lattice spacing. A set of arbitrary lattice planes in a crystal is illustrated in Figure 2.6, separated by the lattice plane distance d. Two X-rays of wavelength λ are incident to the planes with an angle θ. They are reflected off the first and second plane, respectively, again with the angle θ. The second wave has travelled an additional distance $2dsin(\theta)$, as illustrated in Figure 2.6. For the two waves to be in phase after reflection, this path should be equal to a wavelength λ, or a multiple of the wavelength, $n\lambda$. This condition is expressed in Bragg's law as:

$$2d \sin\theta = n\lambda. \tag{2.15}$$

When this condition is met, the reflected waves travel in phase. At the Bragg angle θ, the constructive interference will be at a maximum and so will the amplitude of the reflected waves. The maximum intensity gives rise to a *Bragg peak*. This peak is in the same reciprocal space position as one of the points in the reciprocal lattice. Bragg's law gives the directions of scattering, the Bragg points in reciprocal space, but does not explain the amplitude of the scattered wave.

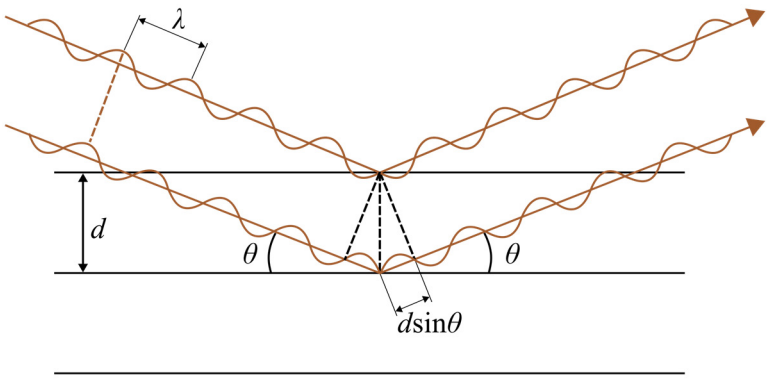

Figure 2.6 Illustration of Bragg's law. Two incoming X-rays with wavelength *λ* scatter off the planes separated by *d*. The waves are incident to the planes with an angle *θ*. The two waves are reflected from the first and second plane, respectively, with a phase shift of 180º. After reflection, the two waves are in phase if the extra path that the second wave travelled is equal to *nλ*.

2.3.3 Laue condition

In a crystal, as discussed above, the electrons are ordered in a periodic lattice and the electron density in Eq. (2.9) can therefore be expanded in a Fourier series in terms of the reciprocal lattice vector $\boldsymbol{G}_{hkl}$ [13]:

$$\rho(\boldsymbol{r}) = \sum_G \rho_G e^{i\boldsymbol{G}_{hkl}\boldsymbol{r}}. \tag{2.16}$$

Inserting Eq. (2.16) into Eq. (2.9) gives the following scattering amplitude for the crystal [13]:

$$A_{crystal}(\mathbf{q}) = r_0 \sum_G \int \rho_G e^{i(\boldsymbol{G}_{hkl}-\boldsymbol{q})\boldsymbol{r}} dV. \qquad (2.17)$$

Clearly, $A_{crystal}(\boldsymbol{q})$ is negligible when $\boldsymbol{q}$ differs from $\boldsymbol{G}_{hkl}$ [13]. This gives the Laue condition for non-vanishing amplitude:

$$\boldsymbol{q} = \boldsymbol{G}_{\mathrm{hkl}}. \qquad (2.18)$$

For a periodic lattice, the scattering amplitude is non-zero only at discrete points. It can be shown that the Laue condition is equivalent to Bragg's law.

2.3.4 Crystal strain: elasticity model

We have so far discussed diffraction from a perfect crystal, but crystals are usually not perfect but distorted in various ways. Before we continue with a description of diffraction from a deformed crystal, we need to define the deformation using the concepts of displacement field and strain.

Generally speaking, strain is a measure of the deformation of a material under a load. In the context of crystals, strain occurs when the crystal is subjected to a load that causes the lattice points to change from their ideal. The deformations that we measure in the nanowires are much smaller than the lattice constants, and therefore we can use a model of linear elasticity. Other types of defects that cause larger deviations, like a missing lattice base point, need another treatment that is out of the scope of this thesis.

What we can measure in a diffraction experiment is not the strain directly but the local displacement. The *displacement field* $\boldsymbol{u}(\boldsymbol{r})$ is a vector field in three dimensions so that a vector describes the displacement with a value and direction at each volume element. The displacement field fully describes the deformation of a crystal so that the atom at position $\boldsymbol{R}_n$ in the perfect lattice, is at position $\boldsymbol{R}'_n$ in the deformed lattice:

$$\boldsymbol{u}(\boldsymbol{r}) = \boldsymbol{R}'_n - \boldsymbol{R}_n. \qquad (2.19)$$

The displacement field can be expressed as three components (u_x, u_y u_z) sometimes referred to as u, v and w. The displacement field gives the relative change in position but is independent of the size of the object being deformed. Strain gives the deformation relative to the original size. The strain components in three dimensions are defined as derivatives of the displacement field in each direction:

$$\varepsilon_{ii} = \frac{du_i}{di}\ , \varepsilon_{ij} = \frac{1}{2}\left(\frac{du_j}{di} + \frac{du_i}{dj}\right), \tag{2.20}$$

where ij = (x, y, z).

Hooke's law, known from calculating the extension and compression of springs in undergraduate physics, also has validity for materials in 3D, where the linear elasticity model has been found to hold for small forces and displacements. Here, the concept of *stress* is related to the force F with $\sigma = F/A$ where A is the cross-sectional area. In the context of 3D materials, the stress as well as the displacement, can have components in all three dimensions. A continuous material under a load can stretch, compress, and shear in three directions. Hooke's law in 3D generalizes to:

$$\boldsymbol{\sigma} = C\boldsymbol{\varepsilon}, \tag{2.21}$$

where $\boldsymbol{\sigma}$ and $\boldsymbol{\varepsilon}$ are 3x3 tensors of stress and strain, respectively:

$$\boldsymbol{\sigma} = \begin{bmatrix} \sigma_{xx} & \sigma_{xy} & \sigma_{xz} \\ \sigma_{yx} & \sigma_{yy} & \sigma_{yz} \\ \sigma_{zx} & \sigma_{zy} & \sigma_{zz} \end{bmatrix}, \boldsymbol{\varepsilon} = \begin{bmatrix} \varepsilon_{xx} & \varepsilon_{xy} & \varepsilon_{xz} \\ \varepsilon_{yx} & \varepsilon_{yy} & \varepsilon_{yz} \\ \varepsilon_{zx} & \varepsilon_{zy} & \varepsilon_{zz} \end{bmatrix}. \tag{2.22}$$

Since $\varepsilon_{ij} = \varepsilon_{ji}$, there are only six components to completely define the strain ($\varepsilon_{xx}, \varepsilon_{xy}, \varepsilon_{xz}, \varepsilon_{yy}, \varepsilon_{yz}, \varepsilon_{zz}$). To map the strain tensor to the stress tensor, the stiffness tensor C is a rank four tensor with 3x3x3x3 dimension matrix with 91 components in total. If there is symmetry in the material, these numbers can be reduced. For example, in an isotropic material, the response to a load is the same, independent of what direction of the load. More symmetry is found in different types of crystal lattices.

The stiffness tensor C depends on the four intertwined properties of Posson's ratio, Young's modulus, and the shear and bulk modulus. If a material expands in one direction, it most often contracts in the orthogonal directions and vice versa. The Poisson's ratio is the ratio between the strain in the direction of the load and the strain normal to the load axis. The Young's modulus is related to the stiffness of the material, it is given by the ratio of stress and strain.

2.3.5 Diffraction from a finite crystal with deformations

As we have seen, the scattering in far field under the kinematical approximation from a sample expressed with its electron density $\rho(\boldsymbol{r})$ is:

$$A(\boldsymbol{q}) = r_0 \int \rho(\boldsymbol{r}) e^{-i\boldsymbol{q}\boldsymbol{r}}\, d\boldsymbol{r}. \tag{2.23}$$

This equation shows that the scattering in the far field is equal to the Fourier transform of the exit-wave at the object described by the electron density $\rho(\boldsymbol{r})$. In the following derivation, we will neglect the term r_0. The derivation below follows Ref. [15], which in turn bases its derivation on early work by Laue [16]. To express the far field scattering amplitude of a crystal under the kinematical approximation, we start by introducing three developments to Eq. (2.23). First, the crystal is finite. Secondly, the crystal lattice is not perfect but strained, which is characterized by a displacement field. The first two points are introduced with the definition of a complex object function:

$$S(\boldsymbol{r}) = s(\boldsymbol{r})e^{i\phi(\boldsymbol{r})}, \tag{2.24}$$

where the shape function $s(\boldsymbol{r})$ is equal to one inside the crystal and zero outside. The phase of the object function is related to the displacement field with:

$$\phi(\boldsymbol{r}) = -\boldsymbol{q}\boldsymbol{u}(\boldsymbol{r}). \tag{2.25}$$

At the Laue condition, where $\boldsymbol{q} = \boldsymbol{G}_{hkl}$, the phase is equal to the scalar product $\boldsymbol{G}_{hkl}\boldsymbol{u}(\boldsymbol{r})$ which is the projection of $\boldsymbol{u}(\boldsymbol{r})$ onto $\boldsymbol{G}_{hkl}$. The third point we want to introduce is that we have a crystal, and the atoms in a crystal is periodic. As we saw in the previous chapter, we can describe the electron density as a set of discrete lattice points. The lattice points in the perfect crystal can be expressed as a sum of Dirac delta functions δ:

$$\rho(\boldsymbol{r}) = \sum_{n=1}^{\infty} \delta(\boldsymbol{r} - \boldsymbol{R_n}), \tag{2.26}$$

where $\boldsymbol{R}_n$ is the positional vector of the *n*th unit cell. If we introduce these three points into Eq. (2.23), the electron density is replaced with an expression that represents a finite crystal with strain, and the unit cell structure factor $F(\boldsymbol{q})$ that is here the same for all unit cells in the crystal:

$$A(\boldsymbol{q}) = F(\boldsymbol{q}) \int \rho(\boldsymbol{r}) s(\boldsymbol{r}) e^{-i\boldsymbol{q}\boldsymbol{u}(\boldsymbol{r})} e^{-i\boldsymbol{q}\boldsymbol{r}}\, d\boldsymbol{r}. \tag{2.27}$$

To simplify this equation, the Fourier convolution theorem can be applied. This states that the Fourier transform of the product of two functions, in this case $\rho(\boldsymbol{r})$ and $S(\boldsymbol{r}) = s(\boldsymbol{r})e^{-i\boldsymbol{q}\boldsymbol{u}(\boldsymbol{r})}$, is equal to the convolution between the Fourier transform of the two functions. This together with the definition of convolution reads:

$$\begin{aligned} \mathcal{F}\big(\rho(\boldsymbol{r})S(\boldsymbol{r})\big) &= \rho(\boldsymbol{r}) * S(\boldsymbol{r}) \\ &= \int \rho(\boldsymbol{q}')S(\boldsymbol{q} - \boldsymbol{q}')d\boldsymbol{q}', \end{aligned} \tag{2.28}$$

where the Fourier transform of the functions $\rho(\boldsymbol{r})$ and $S(\boldsymbol{r})$ is denoted by the change of variable. The scattering amplitude in Eq. (2.27) becomes:

$$A(\boldsymbol{q}) = \frac{F(\boldsymbol{q})}{(2\pi)^3} \int \rho(\boldsymbol{q}')S(\boldsymbol{q} - \boldsymbol{q}')d\boldsymbol{q}'. \tag{2.29}$$

To evaluate this expression, lets look at the two Fourier transforms in turn. The Fourier transform of a perfect crystal is another sum of delta functions:

$$\rho(\boldsymbol{q}') = \sum_n \delta(\boldsymbol{q}' - \boldsymbol{h}_n). \tag{2.30}$$

Where v is the volume of the unit cell and $\boldsymbol{h}_n = 2\pi\boldsymbol{G}_n$, where $\boldsymbol{G}_n$ is the reciprocal lattice vector to the unit cell n. The second Fourier transform is:

$$S(\boldsymbol{q} - \boldsymbol{q}') = \int S(\boldsymbol{r})e^{-i(\boldsymbol{q}-\boldsymbol{q}')\boldsymbol{r}}d\boldsymbol{r}. \tag{2.31}$$

Eq. (2.29) becomes:

$$\begin{aligned} A(\boldsymbol{q}) &= \frac{F(\boldsymbol{q})}{v} \int (\sum_n \delta(\boldsymbol{q}' - \boldsymbol{h}_n) \int S(\boldsymbol{r})e^{-i(\boldsymbol{q}-\boldsymbol{q}')\boldsymbol{r}}d\boldsymbol{r})d\boldsymbol{q}', \\ &= \frac{F(\boldsymbol{q})}{v} \sum_n \int S(\boldsymbol{r})e^{-i(\boldsymbol{q}-\boldsymbol{h_n})\boldsymbol{r}}d\boldsymbol{r}, \end{aligned} \tag{2.32}$$

where in the last step the sifting property of the Dirac delta function is used. This entails that, by definition, the integral of the delta function multiplied with a function is equal to that function at the position of the Dirac delta.

In coherent imaging, we are interested in the distribution around a single Bragg peak $\boldsymbol{h}_n = \boldsymbol{h}$. In the vicinity of a Bragg peak, the scattering vector is $\boldsymbol{q} \approx \boldsymbol{G}_{hkl}$ according to the Laue condition. Introducing a variable describing the distance from the Bragg peak: $\boldsymbol{Q} = \boldsymbol{q} - \boldsymbol{h}$, the scattering amplitude here becomes:

$$A(\boldsymbol{Q}) = \frac{F(\boldsymbol{Q})}{v} \int S(\boldsymbol{r})e^{-i\boldsymbol{Q}\boldsymbol{r}}d\boldsymbol{r}. \tag{2.33}$$

The scattered intensity is the absolute squared of the scattering amplitude:

$$I(\boldsymbol{Q}) = \frac{|F(\boldsymbol{Q})|^2}{v^2} \left| \int s(\boldsymbol{r})e^{-i\boldsymbol{h}\boldsymbol{u}(\boldsymbol{r})}\, e^{-i\boldsymbol{Q}\boldsymbol{r}}d\boldsymbol{r} \right|^2. \tag{2.34}$$

The result from this derivation shows that the scattered intensity in the vicinity of a Bragg point is mainly determined by the Fourier transform of the object function. The object function is determined by the objects shape and the displacement field in the direction of the scattering vector.

The far field diffraction from a perfect infinite crystal consists of Bragg peaks in the form of delta spikes. When the crystal is finite, the intensity around each Bragg peak is symmetrically broadened. The shape of the broadening is reciprocal to the shape of the real space object. For a finite crystal with a strain gradient, there is an asymmetric broadening of each peak that is related to the displacement.

3 The production and focusing of synchrotron radiation

I this chapter, X-ray beams are produced with a synchrotron and focused to the nanoscale.

3.1 Production of X-rays

Three basic mechanisms give rise to X-rays:

i. emission from electronic transitions,
ii. radioactive decay from nuclei, and
iii. acceleration of a charged particle.

The historically most common way to produce X-rays for experiments is with an X-ray tube, where both i and iii contribute to the production. Here, electrons are generated by heating up a filament, that is, by thermionic emission. The electrons are accelerated in an electric field towards a target and two phenomena occur to create X-rays. First, the electrons are quickly decelerated, and the kinetic energy is transferred to X-rays, creating braking radiation (*Bremsstrahlung*). Secondly, some of the electrons will kick out core electrons in the target and the vacancies are filled with higher shell electrons which give fluorescence. The spectra from an X-ray tube is characterized by the material in the anode, which will be a broad peak from the bremsstrahlung together with high intensity fluorescence peaks.

3.1.1 Synchrotron radiation at MAX IV

An X-ray beam produced by a lab source, like an X-ray tube, can fill its purpose in many situations, but synchrotrons can produce X-ray beams with much higher quality in terms of intensity, energy range and *brilliance*; a concept that will be discussed further in this section. MAX IV [17, 18] was inaugurated in 2016 and is the first of the so-called 4th generation of synchrotrons, with a design to produce unprecedentedly high brilliance. So what are the properties of an X-ray beam that

makes the quality high? One valuable quantity is brilliance which can be understood by looking at its units:

$$[brilliance] = \frac{photons}{second \cdot mrad^2 \cdot mm^2 \cdot 0.1\%BW}. \quad (3.1)$$

First, a high flux of the X-ray beam is required, that is, a high number of photons per second. Then follows the requirement of the photons: to increase brilliance, they should have a small bandwidth in energy, they should be localised in a small area, and have low angular divergence, that is, travel uniformly in the same forward direction. Synchrotrons have around 1 mrad divergence, which is a huge improvement to a lab source. Importantly, beyond its much higher brilliance, the fact that the photon energy can be tuned gives synchrotron radiation a critical advantage to the lab source. For diffraction imaging, among other experiments, coherence, which is related to brilliance, is a vital property of the X-ray beams that will be discussed later in this chapter.

Synchrotron radiation can be defined as the electromagnetic radiation emitted by charged particles traveling at relativistic speeds and accelerated in curved trajectories [12]. In a synchrotron, relativistic electrons with constant energy are forced to travel in a circular trajectory by strong magnetic fields. As the electrons are accelerated by changing direction in the magnetic field, they will emit synchrotron radiation. The energy that the electrons lose when emitting synchrotron radiation is compensated for by radiofrequency cavities around the ring.

MAX IV has two storage rings, see Figure 3.1, one smaller designed for a lower electron energy of 1.5 GeV, and a larger ring for higher energy X-ray experiments where the electron energy is 3 GeV. Around the rings are the beamlines, the experimental stations where the experiments take place, each modifying the generated synchrotron radiation to fit the experiments specific for each beamline. The source for the electrons is a linear accelerator (LINAC) where electrons are accelerated to relativistic speeds, up to either 1.5 GeV or 3 GeV, and directed into the respective rings. The LINAC keeps the electron current in the rings constant by filling them up with bunches of electrons (top-up) as the storage rings lose electrons.

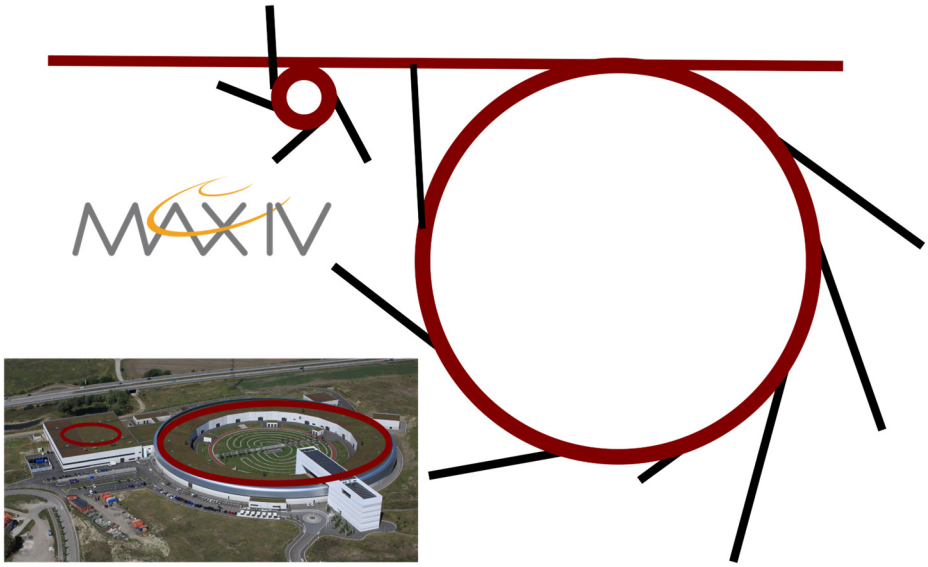

Figure 3.1 A schematic sketch of MAX IV laboratory, with the linear accelerator, the smaller 1.5 GeV storage ring, the larger 3.0 GeV storage ring, and the beamlines. The inset shows a photo of MAX IV. Photo credit www.maxiv.lu.se.

Electrons are kept in their circular trajectory around the rings using a lattice of *achromats*, where each acromat is a collection of magnets of different designs. The achromats include *bending magnets*, bending the trajectories of the electrons, emitting synchrotron radiation in the shape of a cone in the direction of the velocity. In the early history of synchrotrons, the radiation was produced only from bending magnets. Nowadays, most storage rings have straight sections with *insertion devices,* one for each beamline, to produce X-rays of even higher brilliance. The insertion devices are of two types, undulators and wigglers, both based on a series of dipole magnets with alternating polarity that forces the electron beam to bend in a sinusoidal path. The oscillations in a wiggler are larger, resulting in a broad energy spectrum, while the smaller oscillations of the undulator makes the radiation from each oscillation add coherently in a narrow energy range [19].

The brilliance of the X-ray beams will depend on the brilliance of the electron beam, so the design of the achromatic lattice is key. The MAX IV 3 GeV is the first synchrotron source with a diffraction-limited storage ring (DLSR) design [20]. It employs a multibend achromat lattice design, which means, among other things, that there are an additional number of magnets per unit length. This makes it possible to have a much smaller electron beam cross section, which reduces the source size and therefore increases the coherence (see next section). The design of the achromat lattice gives MAX IV its unique properties, which is a great leap in brilliance compared to other sources.

3.2 Coherence

In previous chapters, it was stated that the incident beam was coherent in order to ensure constructive interference from Thomson scattered waves. Here we will go into the subject of coherence a bit deeper. In simple terms, the concept of coherence describes how similar waves are to each other and can be divided into two different quantities: *temporal* coherence and *spatial* coherence. Temporal coherence is how similar the wavelengths are between waves, i.e., how monochromatic the beam is, while spatial coherence describes if the waves are traveling in the same direction or not.

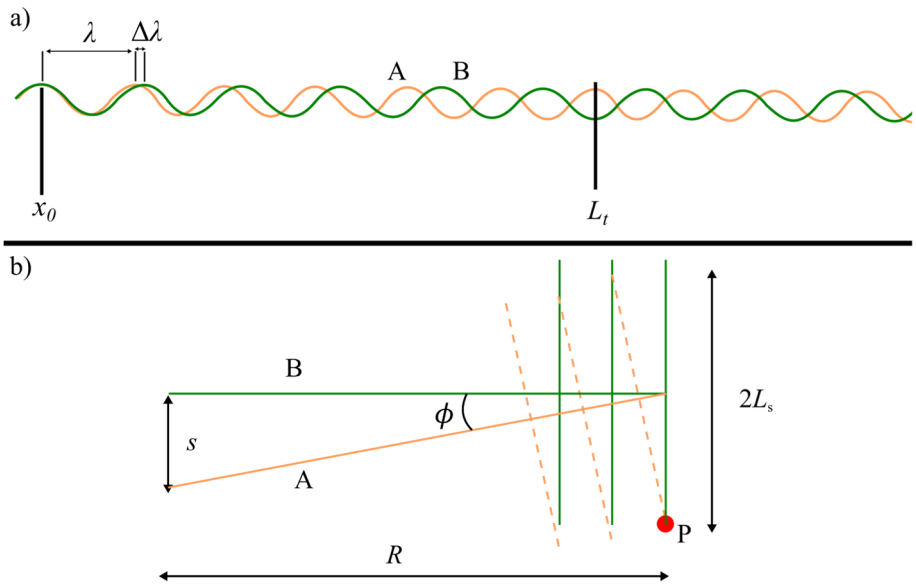

Figure 3.2 Illustration of a) temporal and b) spatial coherence.

In coherent imaging, it is vital to discuss the length scale of the coherence, quantified with the *coherence length*. Say that two waves A and B, with different wavelengths λ and $\lambda + \Delta\lambda$, are in phase at a point x_0, see Figure 3.2 (a). The temporal coherence length is defined by the propagation distance L_t at which the waves are completely out of phase, that is, they have a 180° phase shift. This is related to the wavelengths by:

$$L_t = \frac{\lambda^2}{2\Delta\lambda}. \tag{3.2}$$

The temporal coherence length depends on the monochromator and its deviations from a perfect crystal.

If instead the waves A and B are monochromatic, but travel in different directions from two points separated by a distance *s*, in the directions of a point *P*, see Figure 3.2 (b). At the observation point *P*, A and B are in phase. The spatial coherence length L_s is defined as the distance from point P along the wavefront of A, where A and B are completely out of phase. From geometry, it is evident that $L_s = \frac{\lambda}{2\Delta\phi}$.

For a coherent imaging experiment, the origin of the beam originates from an aperture with an extension *s* and the experiment is performed at a distance *R* from the aperture. It is observed from Figure 3.2 (b) that $sin(\phi) = s/R$, and that for small angles $\phi = s/R$. To relate the spatial coherence length to these quantities, the coherence length can be rewritten as:

$$L_s = \frac{\lambda R}{2s}. \tag{3.3}$$

The magnetic lattice of MAX IV focuses the electron beam to a smaller size than previous generations of synchrotrons, which gives a smaller source size and therefore a longer coherence length. Perfect coherence is not possible; by quantifying coherence with the coherence lengths, we can define how separated two objects can be and still give constructive interference. The important length scale is the size of the sample. For a coherent imaging experiment, the beam should be coherent in the volume of the sample, since incoherence will blur the fringes.

3.3 Focusing of X-rays

Refraction and reflection are closely related to the concepts of scattering but on a macroscopic level. The connection between the two viewpoints is realized in the definition of the refractive index n for X-rays, which is a complex quantity:

$$n = 1 - \delta + i\beta. \tag{3.4}$$

Here, the correction term δ is related to Thomson scattering and β to absorption. For hard X-rays, δ and β are on the order of 10^{-5} and 10^{-6}, respectively. The refractive index for optical light is above one, for example, 1.333 in water, while the real part of the refractive index for X-rays is close to and slightly below unity. This weak interaction can help explain why it is not a straightforward task to focus X-rays. Snell's law gives the relation between the incident light of the refracted light between two media with refractive index n_1 and n_2 as:

$$n_1 \sin\theta_1 = n_2\theta_2, \quad (3.5)$$

where θ_1 and θ_2 is the incident and refracted angle, respectively. For incident media of vacuum, $n_1 = 1$, then then for optical light $n_2 > 1$ which leads to $\theta_1 < \theta_2$. For X-rays, $n_2 < 1$ and $\theta_1 > \theta_2$, which means that the X-rays will refract in the opposite direction compared to visible light. A convex lens focuses optical light but is divergent for X-rays.

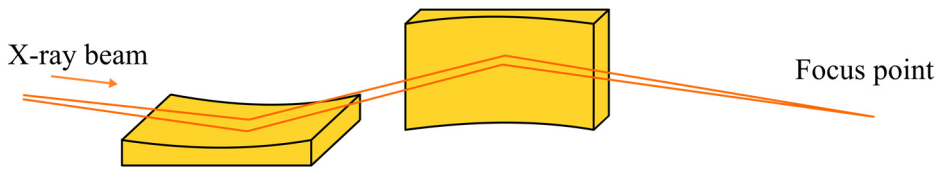

Figure 3.3 A set of KB-mirrors used to create a nanofocus of the X-ray beam. One mirror focuses in the vertical plane and one in the horizontal.

For focusing the X-ray beam to the nanoscale, the focusing optics used in this thesis are Kirkpatrick-Baez (KB) mirrors [21]. These mirrors, shown in Figure 3.3, are a pair of concave mirrors, one focusing vertically and one horizontally, into a single focus point. For the material to work as mirrors for X-rays, the incidence angle must be below the for total external reflection α_{crit}:

$$\alpha_{crit} = \sqrt{2\delta}, \quad (3.6)$$

which is in the order of milliradians. The curvature of the mirrors is slight, allowing the surface to be locally flat and the equation is still valid [12]. The δ in Eq. (3.6) is related to Thomson scattering of the electron density in the material, so the mirrors are coated with a high electron density material such as gold or iridium to increase the critical angle and make it easier to achieve the needed incidence angle.

KB mirrors, or other reflective elements, have the advantage of high efficiency, so very few photons are lost. Another advantage with KB mirrors is that the beam position is the same for all energies, in other words, it is achromatic focusing.

3.4 NanoMAX beamline

The nanowires under investigation in this thesis are in the range of 100 nm in diameter and a few microns in length. To construct an image of such a small entity, a probe that is below 100 nm was required. Both spatial and temporal coherence

need to be ensured to produce coherent diffraction patterns, and a high flux was necessary to provide enough signal. More specifically, the coherence volume needs to exceed the dimensions of the part of the nanowire that is illuminated in one scanning point.

Based on these considerations, the experiment included in this thesis are all performed at the hard X-ray coherent imaging nanoprobe at the NanoMAX beamline [22] at MAX IV. The beamline is found in the larger of the two storage rings of MAX IV, with higher electron energy and lower emittance. The beamline's capabilities include high resolution images from fluorescence and diffraction, creating 2D maps of composition, strain, crystallographic phase of samples typically a few micrometers in size. Techniques include scanning XRD, nano-tomography, Bragg coherent diffraction imaging (BCDI), and ptychography. 3D resolved Bragg ptychography was recently achieved from an experiment at NanoMAX, see Ref. [23]. Further information on the beamline is described in the following references; for a walkthrough of the beamline optics see Ref. [22], a discussion about the coherence see Ref. [24], and on the design and evaluation of the diffraction end station in Ref. [25].

3.4.1 Optics hutch and secondary source

The X-ray beam from the storage ring is polychromatic and divergent. The first conditioning of the beam to fit the experimental requirements takes place in the optics hutch, see Figure 3.4. Here the beam is collimated using slits, and a smaller range of energies is selected with a monochromator. At NanoMAX, the monochromator are two Si(111) crystals that diffracts a bandwidth of wavelengths according to Bragg's law, which defines the temporal coherence of the X-ray beam. Next, the X-ray beam is focused with a set of mirrors to focus the beam vertically and horizontally. The focus of the mirrors is the next component of the beamline, the secondary source aperture (SSA), which is around 25 meters away from the mirrors. The SSA cuts away part of the beam to control the spatial coherence. This acts as a new source for the X-ray beam. The size of the SSA is the source that defines the spatial coherence defined in Eq. (3.3). The beamlines focusing on coherent methods are usually the longest beamlines in a storage ring, as is the case for NanoMAX at MAX IV, to ensure spatial coherence by increasing R in Eq. (3.3). In total, NanoMAX is around 100 meters long.

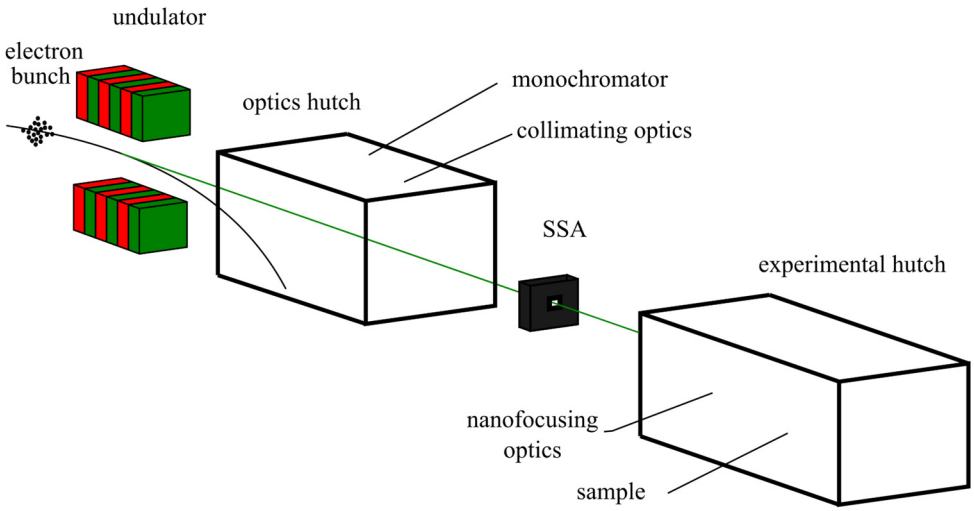

Figure 3.4 Sketch of the NanoMAX beamline. The electron bunches travel through the undulator, where the X-ray beam is generated and directed to the beamline. The beamline consists of an optics hutch, a secondary source aperture (SSA) and an experimental hutch.

3.4.2 Experimental hutch

The experimental hutch is where the nanofocus is created and focused on the sample, and where the experiments take place. At NanoMAX, the experimental hutch is designed to hold two end stations, that is, the beam can be directed into two separate experimental stations with different designs. The first is dedicated to diffraction experiments [25] and uses KB mirrors as a focusing device, while the other uses zone plates that under commissioning but will be an imaging station. We used the diffraction end station in paper I-IV, and this will be discussed further here.

A photo from one of our diffraction experiments at NanoMAX is shown in Figure. 3.5. Here, the X-ray beam is incident from the left and focused by the KB mirrors before it hits the sample. The sample is placed on a scanning stage that consists of a goniometer scanning stage for rough stepping. On top of that is a 3-axis piezoelectric stage. A detector is placed on a robot arm in Bragg geometry, that is, in the Bragg condition for the desired reflection based on the sample. Another detector is placed inline a few meters away from the sample in the forward direction of the beam. The setup also includes a fluorescence detector, which is placed close to the sample to measure as many XRF photons as possible. This setup is regularly used to do high resolution fluorescence mapping, for example in Ref. [26]. To find the position of the sample and placing it in the focus of the X-ray beam, two microscopes are at hand, one placed above, looking down at the sample, the other,

an on-axis microscope looking at the sample from the same direction as the X-ray beam.

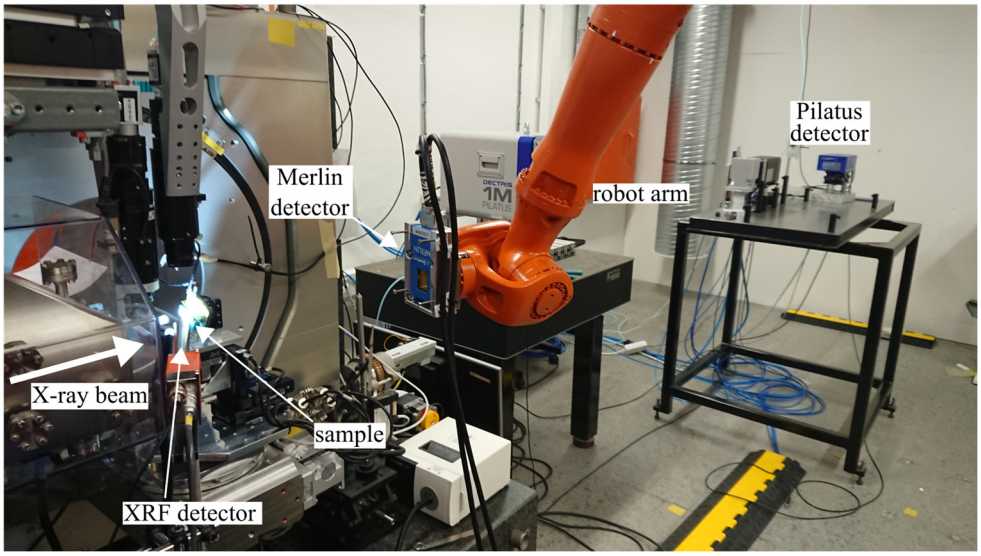

Figure 3.5 Photo of a coherent imaging experimental setup at the NanoMAX beamline around the time of the experiments for this thesis. The X-ray beam is incident from the left and focused by the KB mirrors before it hits the sample. The diffracted beam is measured by a Merlin detector mounted on a robot arm, while the forward beam is detected by the Pilatus detector about 4 meters downstream. A fluorescence detector is placed close to the sample.

With the KB mirrors, the coherent flux can be focused to between 50-100 nm, depending on the energy. The energy can be tuned between 5 and 28 keV [22] and the coherent flux depend on the energy and is $6 \cdot 10^{10}$ photons/s at 8 keV.

We performed the first ever nano diffraction experiment when the beamline was first opened for users in July 2017. I have since been following the development of the beamline and have continuously been visiting for experiments and noticed its advances. In the first experiment, the Bragg detector was positioned in Bragg orientation by placing it manually on a table, measuring the distance with a tape measure. Results from this experiment were published in paper I. Soon after that experiment, a robot was installed to hold the detector. The robot lets the user control the detector position during experiments, while its position is automatically recorded as metadata. Movements of the detector can be scripted in the same way as the scanning stage. More recently, the forward detector has been placed in a flight tube.

4 Strain mapping in nanocrystals

In this chapter, the crystal strain is measured with synchrotron radiation.

4.1 Sources of strain in nanowires

In chapter 2, we saw that strain in a crystal is a stretching or compression of the lattice, such that the lattice points deviate from the ideal lattice points. It can both be a problem to mitigate or prevent, or a source to improve the performance, tailor the properties, for the application to develop new technologies in electronics.

In paper IV, strain is induced by the metal contacts at the two ends of the nanowire, which strains the nanowire locally under the contacts and bends the nanowire. The III-V nanowires in paper I, II and IV are grown from a gold seed particle, and some strain appears locally around the interface of the gold particle. In paper I-III there is strain from a lattice mismatch between the two materials in a heterostructure, as well as variation in lattice spacing from the composition. Other possible sources of strain in nanowires include embedment or other types of processing to fabricate nanowire devices, stress from thermal expansion, mechanical force, or piezoelectric fields.

4.1.1 Strain from a lattice mismatch

A heterostructure is formed from two materials A and B, which generally will have different lattice constants a_A and a_B. There are two types of nanowire heterostructures, core-shell or axial heterostructures. As the name entails, the core shell has a core of material A and the material B is grown as a mantel surrounding material A, while in an axial heterostructure, material A and B are grown on top of each other. At the interface, or *heterojunction*, the lattices need to adjust to form a continuous material. The lattice mismatch is defined as:

$$\epsilon_{mismatch} = \frac{a_A - a_B}{a_A}. \qquad (4.1)$$

For small lattice mismatches, the strain induced by the lattice mismatch can be relaxed *elastically*, see Figure 4.1. Here, the relaxation will be gradual and at some distance from the heterojunction, the lattice will be strain-free. Material B, with the

smaller lattice constant, will have a larger lattice constant compared to its ideal lattice at the interface, while the opposite is true for material A. The lattice in material A will be compressed close to the interface, while material B will be expanded. In other words, material A will be negatively strained while B is positively strained in the direction of *x*. In the direction normal to the interface *y*, the strain is in the opposite direction with magnitude according to Poisson's ratio. For a load along *y*, Poisson's ratio is:

$$\nu = -\frac{\epsilon_{xx}}{\epsilon_{yy}}. \qquad (4.2)$$

The range of ν is commonly between 0.1 and 0.45, where a low value signifies a material that gives little response in other dimensions when stressed in the other. A material like rubber that is largely compressed when stretched in other direction has *v* around 0.5.

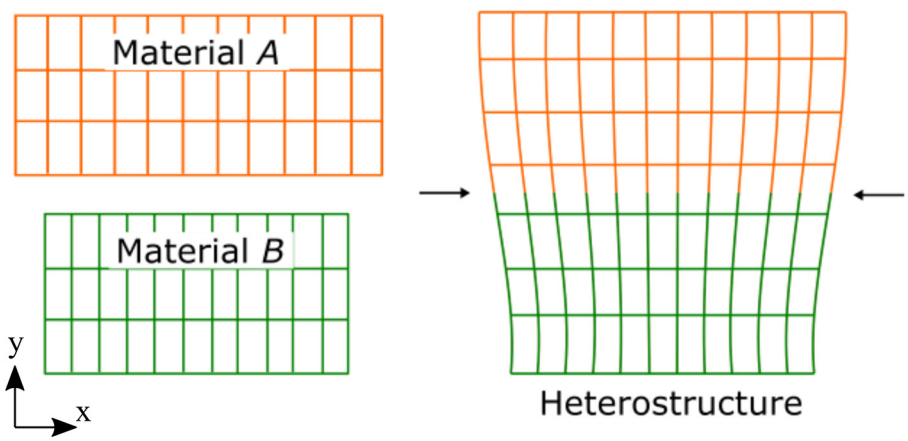

Figure 4.1 A heterostructure is formed from two materials A and B with slightly different lattice constants. The difference between lattice constants is exaggerated in this figure. To the right a heterostructure is formed from the two materials A and B. The interface between the two materials is indicated with two arrows and is referred to as a heterojunction.

For larger mismatches, there can be *plastic* accommodation, which means that dislocations will form [27]. Then the two lattices are matched by the exclusion of some lattice points in one lattice. There can also be strain in combination with dislocations. Whether the stress is relaxed elastically or plastically, depends on the dimensions of the heterostructure and the magnitude of the mismatch. Plastic accommodation is, in general, something that should be avoided when building electronic devices, as dislocations are centers for carrier recombination.

The major part of this thesis is dedicated to axial heterostructures, where segments of different lattice parameters are put together axially to form the nanowire. The

lattice mismatch is along the radial dimension, and is therefore the most interesting part of the strain tensor. However, since the axial and radial part of the strain tensor are related to each other with the Young's modulus under the model of linear elasticity, both are to an approximation accessible when one is measured. This is thoroughly investigated with a FEM COMSOL model in paper I, describing the result from both the axial and the radial strain distribution. Since the nanowires are thin and elongated objects, the axial part of the strain tensor is the orientation that creates the smallest amount of averaging in a measurement, explaining why we have chosen to measure the axial reflection in all publications.

4.2 Scanning X-ray diffraction

With lab sources, X-ray diffraction can be used to study nanowires in the form of averages over ensembles [28, 29], since the beam is large and covers a collection of nanowires. This gives statistical information about the crystal structure and morphology. With the developments in nanoscale focusing of X-rays and the high photon flux from synchrotron sources now available [30], it became possible to image single nanowires with a focused X-ray beam combined with scanning [31, 32]. This technique has been used to create images of morphology and strain of nanowires and nanowire devices with spatial resolution 50-100 nm and a strain sensitivity of 10^{-4}-10^{-5} [33-40].

In scanning X-ray diffraction, we do not access the shape function or the displacement field directly. Instead, we illuminate a 3D volume of the object in each scanning position and assume that the lattice spacing inside is uniform and fulfils the Bragg condition at a single $\boldsymbol{G}_{hkl}$ value. The shift of the reciprocal lattice vector depends on strain and tilt and is illustrated in Figure 4.2, with a lattice spacing d in Figure 4.2 (a) that is related to a reciprocal scattering vector $\boldsymbol{G}_{hkl}$. If the crystal is compressed uniformly, to create a new lattice spacing d, shown in Figure 4.2 (b), the reciprocal lattice is extended in the same direction. The Bragg condition will be fulfilled at a slightly different angle θ. If the lattice is tilted, as shown in Figure 4.2 (c), the Bragg peak will also shift. Strain changes 2θ and θ, but tilt only changes θ. The task in the analysis of scanning XRD is to track these small shifts of the Bragg peak for each real space grid point.

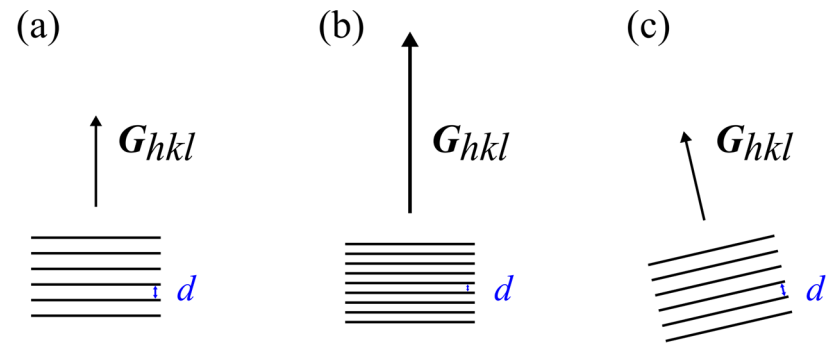

Figure 4.2 A set of planes in a lattice with the lattice spacing d and reciprocal lattice vector $\boldsymbol{G}_{hkl}$. The lattice is uniformly compressed in (b) and tilted in (c), leading to changes of the reciprocal lattice vector.

4.2.1 Experimental setup

Figure. 4.3 shows the principle behind a scanning diffraction setup with a nanofocused beam. This description is general for the experimental setup in paper I-IV, including the Bragg ptychography.

We use a sample holder designed to hold membranes or chips for nanowire devices. The nanowires are scattered with random orientation flat on the substrate in paper I-III, lying flat on Si_3N_4 membranes. In paper IV, single nanowire devices with electrical connections were mounted on the sample holder. The sample holder is placed on the beamline's sample scanning stage that can be translated in x and y, as well as rotated around its axis, and it has a manual rotation around the optical axis. Scanning with the actual X-ray beam is not usually done in a synchrotron experiment since it is too elaborate compared to translating the sample. To translate a sample with high accuracy on the scale of nanometers, piezoelectric stages are commonly used. For faster acquisition, the translation can be done in fly-scanning mode [41], which entails translating the sample in a continuous motion while acquiring diffraction images at a determined rate. This will slightly blur the images, but on the other hand, the measurement can be more stable as the motors do not have to settle down between measurement points.

For the measurements, the nanowire is first aligned with optical microscopy, forward contrast imaging or fluorescence mapping. Single nanowires are usually found with fluorescence mapping. When a single nanowire is identified, we rotate it manually on the sample holder so that it is vertical in the X-ray beam. Next, it is placed in the beam focus. For the rocking curve measurement, it is important that the nanowire is in the center of rotation of the rotational stage.

A diffraction detector is placed in Bragg geometry, that is, at an angle 2θ from the incident X-rays, to match the Bragg condition of the nanowire. The detector used in Bragg geometry in this thesis is a Merlin detector with 55 μm pixel size. The Bragg

peak has an extension in 3D of which two dimensions are sampled by the two dimensions on the detector. The third dimension is reached by rotation the sample slightly along the so-called rocking curve. The sample is rotated in small steps of rotation to cover the whole Bragg peak, which is usually covered in a few degrees.

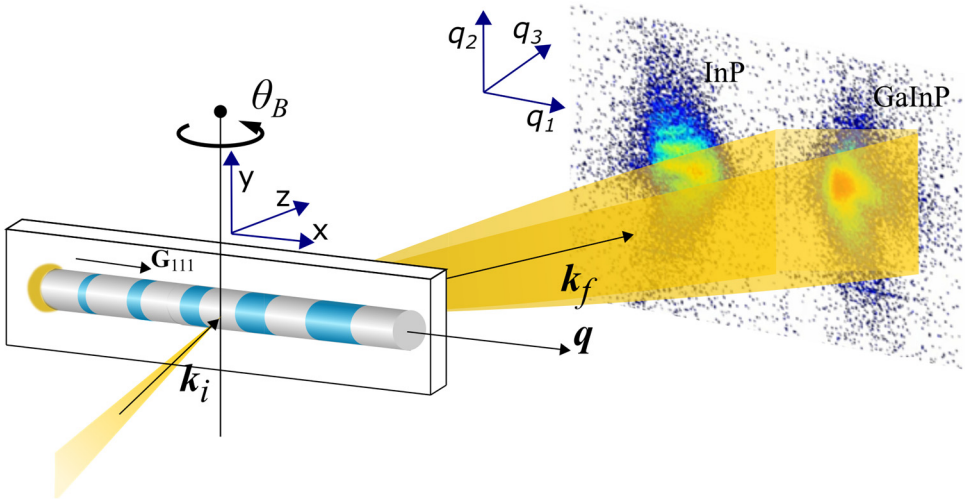

Figure 4.3 Sketch of the experimental geometry.

4.2.2 Analysis

A reminder of the sensitivity of these techniques is reached, when considering that even entering the experimental hutch causes the thermal environment to fluctuate such that a shift is visible in the nanowire images. Thermal movements have usually settled after a day of not entering the beamline hutch, and that is most often when we acquire the best rocking curve data sets. Misalignment can also arise from real space shifts from rotation of the sample. The shifts are compensated for e.g., by observing the nanowires position in the XRF maps.

By summing up the diffraction image on the 2D detector to an intensity number, an intensity image, showing the morphology of the sample, is created. To create an image of the lattice strain and tilts is a more elaborate procedure. The analysis at large entails building up the correct reciprocal space for the collection of 3D diffraction images. First of all, for absolute values of lattice spacing, a calibration of 2θ with a sample of well known lattice parameters is needed. If only relative strain is interesting, the estimate of 2θ from the detector robot position is enough. For more precision, 2θ can be calibrated with a sample of known lattice spacing, e.g., a Si powder. To put axes on the detector images, we need to define the reciprocal pixel sizes $dq_{1,2,3}$. These are related to the real space pixel sizes $\Delta_{1,2,3}$,

where $\Delta_{1,2}$ are the pixels on the detector and Δ_3 is the angular spacing between rotations in radians, with:

$$dq_{1,2} = \frac{2\pi\Delta_{1,2}}{z\lambda}, dq_3 = \frac{4\pi\Delta_3 \sin(\theta)}{\lambda}, \quad (4.3)$$

where z is the distance between sample and detector, λ is the wavelength of the X-rays, and θ is the Bragg angle. For each rotation, the Bragg peak is sliced, not orthogonally, but with the angle θ. That means that the measurement, or *natural*, coordinate system (q_1,q_2,q_3) is not orthogonal, but the axes q_1 and q_3 are dependent on each other, but independent of q_2. The next step in the analysis is to calculate the Bragg peaks position by a center of mass calculation, which is not straight forward to do in the natural coordinate system. To this end, the data is transformed to orthogonal coordinate system (q_x,q_y,q_z) and the axes is recalculated from a natural to an orthogonal system with:

$$\begin{aligned} q_{\mathrm{x}} &= q_1 \cos(\theta), \\ q_y &= q_2, \\ q_z &= q_3 - \sin(\theta). \end{aligned} \quad (4.4)$$

In the orthogonal system, the position of the Bragg peak is calculated using the center of mass, resulting in three coordinates connected to each scanning position. From that, the lattice spacing d in each scanning position is calculated from Eq. (2.13) and the lattice tilts are calculated with:

$$\alpha = \sin^{-1}\frac{q_y}{|\boldsymbol{Q}|}, \quad (4.5)$$

and

$$\beta = \tan^{-1}\frac{q_x}{q_z}. \quad (4.6)$$

The angles are illustrated in Figure 4.4, for the experimental setup in Figure 4.3.

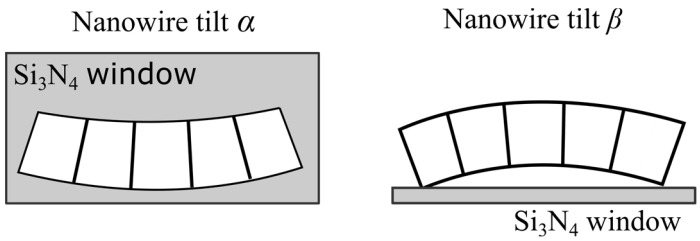

Figure 4.4 Illustration of the lattice tilts α and β in the experimental setup.

Using a fully coherent beam, the information that is encoded in the extension of the Bragg peaks is not directly utilized in scanning X-ray diffraction, and the illuminated volume in one measurement point gives an average value. The resolution is limited by the size of the beam, and furthermore, there is no resolution in the direction of the X-ray path. These limitations can be overcome in the field of coherent diffraction imaging where the diffraction images are inverted to real space.

4.3 Coherent diffraction imaging

4.3.1 The phase problem

Coherent imaging methods have been developed to circumvent the limitation of spatial resolution set by the focusing optics. In chapter 2, we saw how, for a coherent plane wave incident on an object, the exit wave propagated to the far field is related to the object via the Fourier transform. If one could measure the propagated exit wave in far field, the object could be found by inverting it to real space. However, what is acquired is a sampled image of the *intensity* of the propagated exit wave, which is the modulus squared of the complex-valued scattering amplitude:

$$I(\boldsymbol{q}) = |A(\boldsymbol{q})|^2, \tag{4.7}$$

and the phase of the exit wave is cancelled out. A modern X-ray pixel detector can acquire images at a rate of around 1000 frames/second, to be contrasted with the frequency of X-rays which is around 10^{18} Hertz. Thus, one cannot directly measure the phase of the complex scattering amplitude, which is referred to as the *phase problem*.

Coherent imaging methods serve to, in different ways, get back the information about the object that is lost in the diffraction images. In conventional microscopy imaging, the image of the object is formed by an objective lens. For focused X-rays, there are analogous approaches that use a second focusing elements after the object to form an image, but this will hamper the intensity and the resolution of the image.

An alternative route is to recover the phase in an iterative procedure known as *phase retrieval*. This entails measuring the scattered intensity $I(\boldsymbol{q})$ and, by oversampling the signal, retrieving the phases with an algorithm. In the context of imaging, this is sometimes called lens-less imaging, as in contrast to conventional microscopy that uses lenses to form the image. All the diffraction should take place within the coherence volume [14], otherwise, the phases and their interference will be smeared out.

The experimental phase problem was first addressed and solved in crystallography and later adapted to non-crystalline samples with coherent diffractive imaging (CDI). This started with the realization made by Sayre [42] that an object can be reconstructed from the magnitude of its Fourier transform if it is sufficiently oversampled. Finerup showed in Ref. [43] that an object could be reconstructed from diffraction patterns using phase retrieval, which was first experimentally demonstrated by Miao et al. [44].

The principles behind a phase retrieval algorithm for a finite sample is seen in Figure 4.5, where I follow the notation of Ref. [45] in which different algorithms are compared. The object is represented with a complex object function denoted *g*. The algorithm finds the object function that best agrees with the intensity. To do this, the algorithm needs additional information about the object. These "real space constraints" can be e.g., the size or thickness of the object. The fundamental constraint is that the object is non-negative [43]. Often one talks about a 'support of the object' as a constraint, which is just a boundary around the object where the object is fully enclosed. The "Q-space constraints" are the measured intensities of the diffraction $I(\boldsymbol{q})$.

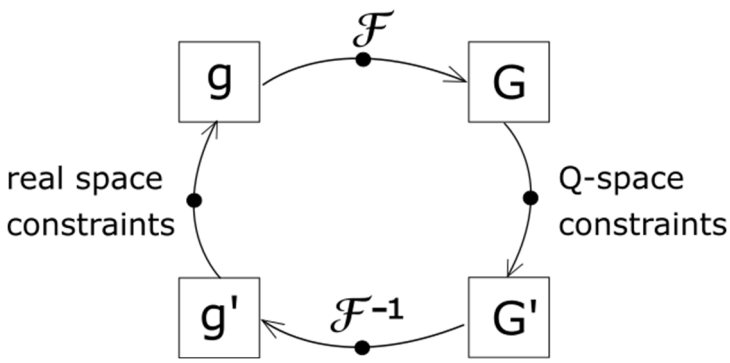

Figure 4.5 Flow chart of a generic phase retrieval algorithm (error reduction approach).

The starting point for the algorithm is an initial guess of the object function *g*, for example, random numbers between $-\pi$ and π in the phase and the amplitude equal to ones. One iteration follows four steps:

1. The object function g is Fourier transformed to Q-space; $\mathcal{F}\{g\} = G$.
2. The Q-space constraints are applied to G, that is, the amplitude is replaced with $\sqrt{(I)}$, to produce G'.
3. G' is inverse Fourier transformed to produce g': an updated guess of the object function
4. The real space support is applied to g' to form g

With this, one iteration loop is fulfilled. When G conforms with the Q-space constraint, that is when $G' = G$, the algorithm has converged to a solution. The same basic principles are behind most phase retrieval algorithms.

Most of the different version of the algorithm concerns step 4; how the real space constraints are applied and how the object is updated. The input-output approach [43] and the hybrid input output (HIO) [45] take the previous iteration into account when applying the real space constraint.

4.3.1.1 Phase wrapping and phase ramp

If the phase $\boldsymbol{u}(\boldsymbol{r})\boldsymbol{G}_{hkl}$ is larger than the range (-π, π), the reconstructed phase will be wrapped. That is, values that are larger than π, will wrap around and result in the phase -π. This can be corrected for by identifying where two adjacent pixels differs with more than π, and add 2πn, for an integer n, to the second pixel.

The phase ramp comes from the property of the Fourier transform that a translation (shift) in real space of $d\boldsymbol{r}$ will result in a phase ramp in reciprocal space:

$$\mathcal{F}\{O(\boldsymbol{r} + d\boldsymbol{r})\} = e^{-i\boldsymbol{q}d\boldsymbol{r}}\mathcal{F}\{\mathrm{O}(\mathbf{r})\}. \qquad (4.8)$$

The reverse is also true, and this can cause issues in coherent imaging. If the diffraction that is to be inverted is not centered correctly, this will cause a phase ramp in the reconstructed image. There will be a phase ramp of 2π for each pixel by which the diffraction is shifted from its center. This can be corrected for by identifying the phase ramp over the image and multiplying the image with the complex conjugate phase term.

4.3.2 Coherent imaging techniques

The initial way to ensure oversampling of the diffraction patterns in CDI, is to illuminate the object with a probe larger than the object. This severely limits the size of objects that can be investigated. Ptychography is an extension to CDI that combines coherent imaging with scanning microscopy. For X-rays it was first implemented in forward geometry by Rodenburg et al. [46] to meet the requirements of extended objects. Ptychography also has the advantage of faster convergence,

since there is a larger redundancy of data and the scanning itself gives spatial information about the sample, and it can give more robust reconstructions by being better at avoiding local minima in the phase retrieval algorithm. In ptychography, the object is scanned with a probe smaller than the object, see Figure 4.6. Oversampling is ensured by measuring the diffraction of overlapping positions with typical probe area overlap of 60-80% [47]. Here, the exit wave after the sample is the product of the object function and the incident beam function. To meet this, we introduce a function for the probe, $P(\boldsymbol{r})$ and describe the exit wave as:

$$\Psi_j(\boldsymbol{r}, \boldsymbol{r_j}) = \mathrm{O}(\boldsymbol{r}) \cdot P(\boldsymbol{r} - \boldsymbol{r_j}), \tag{4.9}$$

where $\boldsymbol{r_j}$ is the relative distance between the sample and the illumination. The propagation to the far field is, like before, given by a Fourier transform.

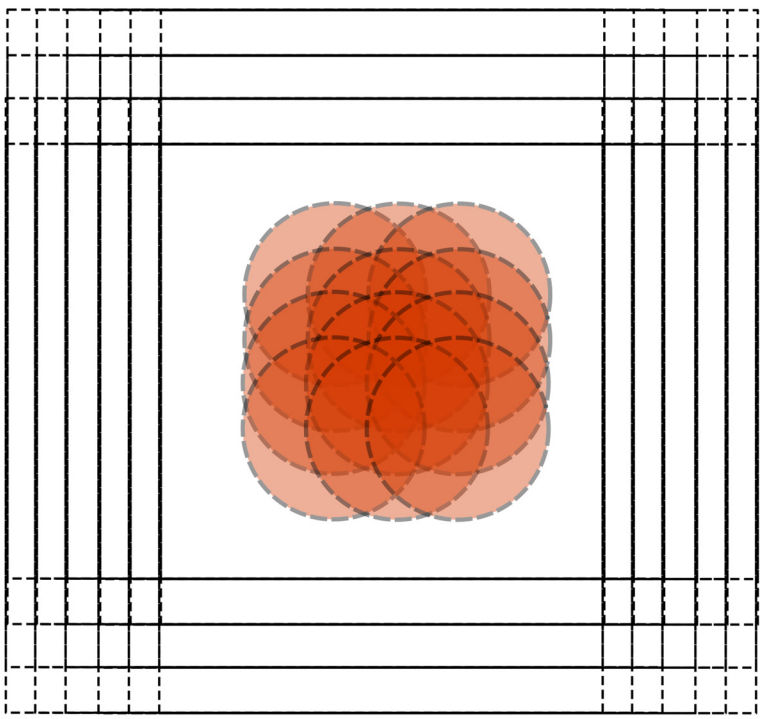

Figure 4.6 Scanning pattern in ptychography. The outer line designates the measurement field of view, and the red circles the beam.

To reconstruct a ptychographic data set, the phase retrieval algorithms must be modified. The first attempt to this end was the ptychographic iterative engine (PIE) [48]. This is an extension to ER, in which an outer loop goes through all scanning positions and diffraction patterns, and the inner loop performs the ER. A refinement

of the PIE algorithm is the extended PIE (ePIE) algorithm [49], which is used extensively in this thesis. Also used in this thesis is the difference map (DM) algorithm, developed for ptychography by Thibault et al. [50, 51]. In ptychography, both the object and the probe can be reconstructed simultaneously [49, 51] with some of the algorithms developed, e.g., the DM and ePIE algorithms.

The Fourier transform gives the contributions of spatial frequencies in the object. The larger frequencies are in the middle and the smaller frequencies are at the edges. How large part of the diffraction pattern is used in the phase retrieval algorithm that is used, sets a limit to the spatial resolution of the reconstructed object. The limit on resolution is set by how high frequencies can be resolved. The pixel size in the retrieved image is given by Eq. (4.3).

4.3.2.1 Coherent imaging in Bragg geometry

In Bragg geometry the detector and the crystalline object are oriented with respect to the beam such that Bragg's law is fulfilled. In this geometry, the coherent imaging techniques are sensitive to the displacement field as described in chapter 2. Instead of 2D projections of the Bragg peak, here the 3D Bragg peak is measured in each scanning position and inverted to real space. The phase retrieval algorithms for ptychography developed for transmission geometry can be generalised to three dimensions. In the Bragg geometry, the techniques are referred to as BCDI and *Bragg ptychography*. The measured intensities are described by Eq. (2.34) and the strain is calculated from the phase of the complex reconstructed object with:

$$\boldsymbol{\varepsilon}_{xx} = \frac{\partial u_x(\boldsymbol{r})}{\partial x} = \frac{1}{|\boldsymbol{G}_{111}|}\frac{\partial \boldsymbol{\phi}(\boldsymbol{r})}{\partial x}. \tag{4.10}$$

The Bragg counterpart to CDI, that is sensitive to the displacement field, was first demonstrated by I.K Robinson et al [52] and has since been used extensively to investigate crystalline materials [53-55]. Although the technique has been used for nanowires [56-59], it does not suit the nanowire shape as the technique requires that the whole object is illuminated so well, and it has not been used in this thesis.

Ptychography was extended to work in the Bragg geometry with Bragg ptychography [23, 60-63]. The measurement basics are equal to the one described for scanning X-ray diffraction in section 4.2.1, with the addition of the requirement of oversampling via overlapping measurement points, and finer spacing on the rocking curve. Typical resolutions are 10-50 nm and strain sensitivity 10^{-4}. Successful demonstrations have been mostly limited to test samples. The Bragg ptychography approach sets very high demand on the setup stability, in terms of accuracy in scanning position and angle of rotation, and low vibrations [14]. At every angle along the rocking curve, the scanning positions must align. Furthermore, the long term stability of the sample, affected by e.g., thermal drifts

and high radiation dose, is important since the many positions in ptychography increase the measurement times to typically a few hours.

To address these difficulties, steps have been taken towards unravelling what happens if a single angle of the diffracted 3D ptychographic measurement is reconstructed. A 2D formalism of Bragg ptychography has been developed; Bragg projection ptychography (BPP) [64-68]. There are two alternatives; a 2D version have been developed for thin films, with no phase gradient in the third direction [69] and a 3D version where not all but a set of projections are used, multi angle Bragg projection ptychography (maBPP), which resolves phase variations in 3D [68]. Given a complex 3D object and its 3D Fourier transform, it is known from the projection slice theorem, also known as the Fourier slice theorem, that a 2D slice of the 3D Fourier transform is related to a projection of the complex object.

In order to enable the reconstruction of a the projected complex object function from 2D diffraction images, just like what is done in transmission ptychography, there are conditions on the object including that the projected object and probe should be separable [69]. This is true when the variation along of the structure factor along $\boldsymbol{k}_f$ is negligible [69]. Such projections have been used to prove the validity of a FEM model with high resolution in Ref. [66]. If a slice is taken away from the Bragg condition, where the deviation is described with $\Delta\boldsymbol{q} = \boldsymbol{q} - \boldsymbol{G}_{hkl}$, a phase component is introduced to the scattered intensity [66, 67, 70]:

$$\mathrm{Q}_\theta = e^{-i\boldsymbol{r}\Delta\boldsymbol{q}}. \tag{4.12}$$

This is introduced to the scattered intensity as [68]:

$$I_{j(2D)} = \left|\mathcal{F}\left(RQ_\theta\Psi_j\right)\right|^2, \tag{4.13}$$

where I have used operator formalism following Ref. [68]. Here, R is the projection operator is an integral over the exit wave along the diffracted beam $\boldsymbol{k}_f$. At the exact Bragg angle, Q_θ = 1, a reconstructed 2D Bragg ptychography angle can be considered a projected image of the object.

5 Insights from nanowire strain mapping studies

In this chapter, the highlights from the nano-diffraction experiments on nanowires are discussed.

This thesis concerns X-ray diffraction methods to measure strain and tilt distributions in nanowires. The strain and tilts originate from different sources, including lattice mismatch from heterostructures, metal contacts in nanowire devices, ferroelastic domains, and strain from the growth process. In this chapter, all projects will be discussed in turn.

5.1 GaInP-InP barcode nanowires

Semiconductor materials play a central role in modern electronic devices. The most common semiconductor material is Si, which has over 90% of the solar cell market. III-V semiconductors (e.g., InAs, GaAs, InP and GaP) have a few advantages to Si, including direct band gaps, high charge carrier mobility and tuneable band gaps. These are major advantages in devices that convert light into energy and vice versa, such as light emitting diodes, solar cells, photodiodes, and laser diodes and electronics. For example, III-V based solar cells have achieved a conversion efficiency of 47.1% [71]. Nanowire heterostructures have unique properties that pave the way for interesting applications in photovoltaics [4, 72, 73], light-emitting diodes [74-77], and electronics [78-81]. With precise control of the growth conditions, very sharp heterostructure interfaces can be created.

The materials system first probed with nano X-ray diffraction in this thesis are single InP/$Ga_xIn_{1-x}P$ nanowire axial heterostructures, with multiple InP segments of varying lengths, all below 200 nm. $Ga_xIn_{1-x}P$ is promising within the field of photovoltaics [82], as the bandgap can be tuned from the near-infrared region to the middle of the visible spectra, depending on the composition x. The heterostructure with segments of different sizes provides a good template for testing coherent X-ray diffraction techniques and their limitations and strengths. Moreover, these studies investigate how the strain distribution and lattice tilt vary depending on the lengths of the segments. One of the observations in this thesis is that the results from strain

mapping on heterostructured III-V nanowires indicate that the strain distribution in some situations can be simulated with a linear elasticity model using FEM, discussed in section 5.13.

The nanowires were grown by the group of Magnus Borgström at Solid State Physics, Lund University, starting from arrays of gold particles using metal-organic vapor phase epitaxy, where they grow layer by layer from under the particles to lengths of 2-3 µm. After growth, they were transferred with a lab tissue onto a fresh Si_3N_4 substrate. The nanowires consist of five InP segments of varying lengths within a $Ga_xIn_{1-x}P$ nanowire with a diameter around 180 nm, as shown in a sketch in Figure 5.1 (a). The nanowire in Paper II is from the same sample but has slightly different segment lengths, differing by about 10%. The average amount of Ga in the nanowire was estimated to be x = 21% in paper I, resulting in an initial lattice mismatch between the two types of segments of about 1.5%.

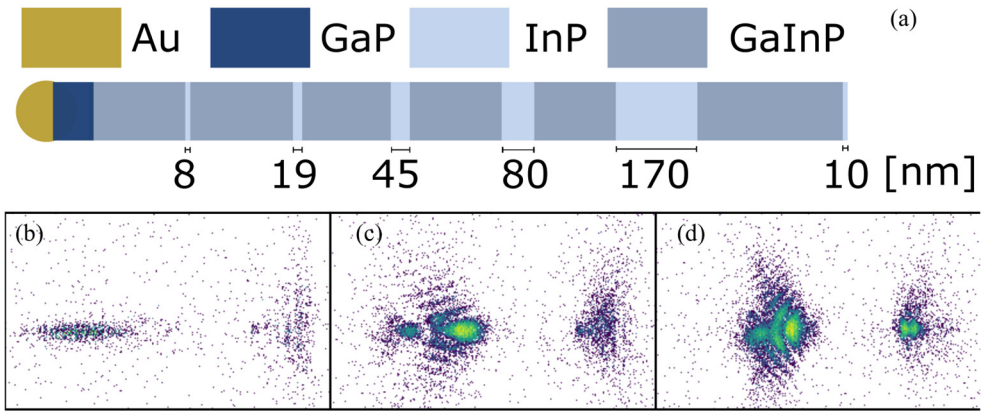

Figure 5.1. (a) Sketch of the nanowire heterostructure (b)-(d) Three examples of single frame diffraction from the three segments of the GaInP/InP barcode nanowire at a Bragg angle close to the InP Bragg condition using a 90 nm X-ray beam.

Three examples of single diffraction frames from three scanning positions along the nanowire is seen in Figure 5.1 (b) – (d). The probe has full width half maximum of 90 nm. Two Bragg peaks are observed in each frame, which originate from InP to the left and $Ga_xIn_{1-x}P$ to the right. The Bragg angle here is close to the Bragg condition of InP, explaining why the right peak is weaker. In (b) the scanning position is close to the center of the smallest 8 nm segment, in (c) close to the 80 nm segment and in (d) close to the largest 170 nm segment. Structural information can be gathered already at this stage from observations of the diffraction patterns. Clearly, InP has higher lattice spacing than GaInP, since the length of $\boldsymbol{G}_{hkl}$ is inversely proportional to the lattice spacing d_{hkl}. The peaks' average separation in q_1 gives a rough estimate of the relative lattice spacing. Furthermore, the asymmetric shape of the Bragg peaks shows that the segments are strained, see further discussion

in section 5.1.3. The smallest 8 nm segment has the largest extension in reciprocal space and the fewest atoms that can scatter the X-rays.

5.1.1 Scanning XRD

In paper I, we investigated the strain distribution in this system with a nanofocused X-ray beam using scanning XRD. This was the first strain mapping result using a diffracted-limited storage ring, coming from the first implementation of a diffraction-limited storage ring at MAX IV laboratory. The early user experiment was done in June 2017, the year the NanoMAX beamline first opened up for user experiments. This was one of the more complex user experiments since it is using a diffraction setup, which requires a combination of excellent spatial precision, high focusing capabilities and a high flux.

The main findings are the strain maps that are shown in Figure 5.2 together with simulated strain maps based on a linear elasticity model, calculated with FEM. Here, we used a probe focus size of full width half maximum of 90 nm. The nanowire was scanned with a step size of 40 nm and 30 nm, in the vertical and horizontal direction, respectively, defining the pixel sizes in the strain and tilt maps.

We observe strain variations as small as 10^{-4}. The largest segment shows a complex strain distribution, where the lattice mismatch at the heterostructure interface leads to a dome-shaped distribution of axial strain in a single segment and a sign shift between positive and negative strain. The dome-shaped strain distribution is most pronounced in the α-tilt, where it produces a vertical shift between negative and positive tilt. The smallest segment is more uniformly strained towards the GaInP structure. The overall similarity with the results from FEM, Figure 5.2 (b) shows the validity of using the linear elasticity model for the system.

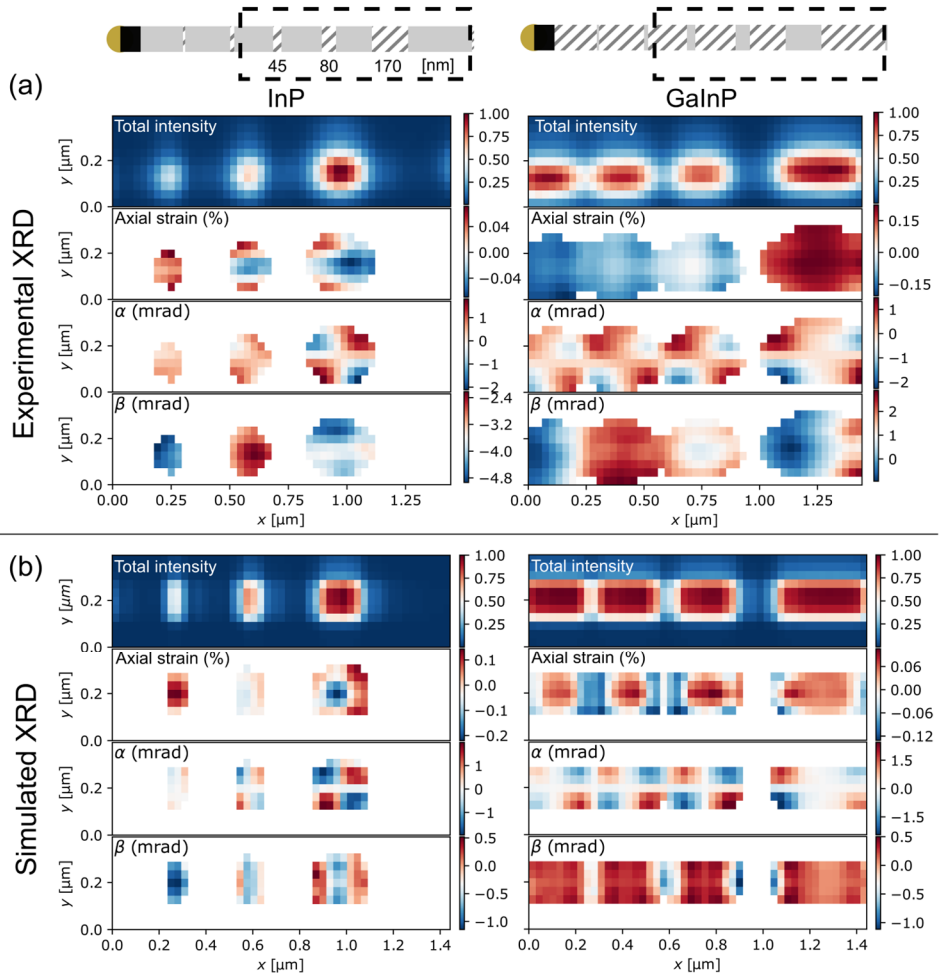

Figure 5.2 (a) Experimental strain mapping of a single axial heterostructure. (b) Simulated strain mapping of a single axial heterostructure. The InP analysis is to the left, and the GaInP analysis is to the right. Figure from paper I.

5.1.2 Bragg projection ptychography

In paper II, we take on the BPP approach and apply it to the barcode nanowires, in order to improve the spatial resolution in two dimensions. The measurement is in principle similar to the scanning XRD, but the coherent imaging technique sets high demands on the beamline's coherent flux, precision in the spatial translation and rotation, beam stability and sample environment stability. We used a larger beam, 180 nm, in order to provide sufficient overlap. When a 3D Bragg ptychography set is measured, all data to perform scanning XRD is there, and it is beneficial to perform as an initial and comparative analysis. The scanning XRD object could be

used as a starting point, or as real space constraints, for a Bragg ptychography phase retrieval reconstruction.

Although there are examples of Bragg ptychography where both the object and beam have been reconstructed [63], it most often requires knowledge of the beam since it is focused and cannot be considered as a plane wave. To this end, the beam is constructed from a measurement with ptychography in forward geometry [51], usually on a test sample. The probe reconstruction used in the BPP reconstruction is seen in Figure 5.3, where phase is encoded in the colour and amplitude as hue. Here, the sample was a Siemens star test sample which was placed 800 µm from the focus spot. The ptychography reconstruction gives the probe in the sample plane, shown in Figure 5.3 (left), and the focus plane was found by propagating the probe in the near field using a near-field propagator in PTYPY [83], shown in Figure 5.3 (right).

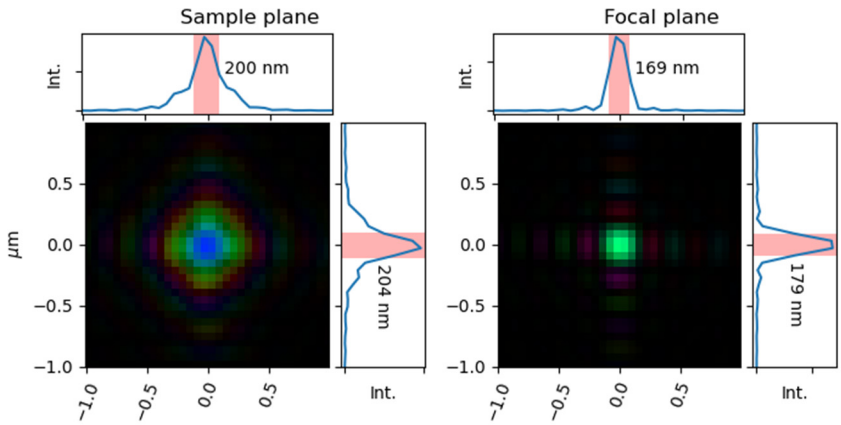

Figure 5.3 Probe reconstruction used in the BPP reconstructions.

A complete barcode nanowire with five InP segments was analysed with BPP, scanning XRD and compared to a FEM model, shown in Figure 5.4. Here, the axial strain is measured. The simulated strain, averaged over the $\boldsymbol{k}_f$ direction is shown in Figure 5.4 (a). The result from scanning XRD is shown in Figure 5.4 (b). The segments have different Bragg conditions, due to the varying strains at different segment lengths, and in addition, a small bending of the nanowire. The amplitude and phase where reconstructed for the five segments, at their respective Bragg peak. The strain was calculated from the phase derivative along x according to Eq. (4.10). The result from each segment was collected in Figure 5.4 (c). BPP analysed from simulated diffraction patterns based on a FEM model is shown in Figure 5.4 (d). As there is no bending included in the FEM model, the Bragg angles are not the same in the experimental and simulated BPP.

The pixel size in the scanning XRD map is given by the step size of the lateral scanning positions, 50 nm, but the resolution is limited by the size of the beam focus, 180 nm. The general trend is that the smaller segments are on average more tensile strained in the axial direction, but the resolution is not enough to resolve differences within segments. The resolution is lower compared to the prevision experiment in Figure 5.2, because the probe focus is larger on account of the BPP overlap.

The BPP successfully reconstructed all segments, even the 9 nm one. The BPP gives better agreement with the FEM model than the scanning XRD. Quantitatively, the strain variations are one order of magnitude too small with scanning XRD while the BPP maps are in better agreement with simulations. The two largest segments have a sign switch, in line with the simulation, not visible in the scanning XRD at this resolution.

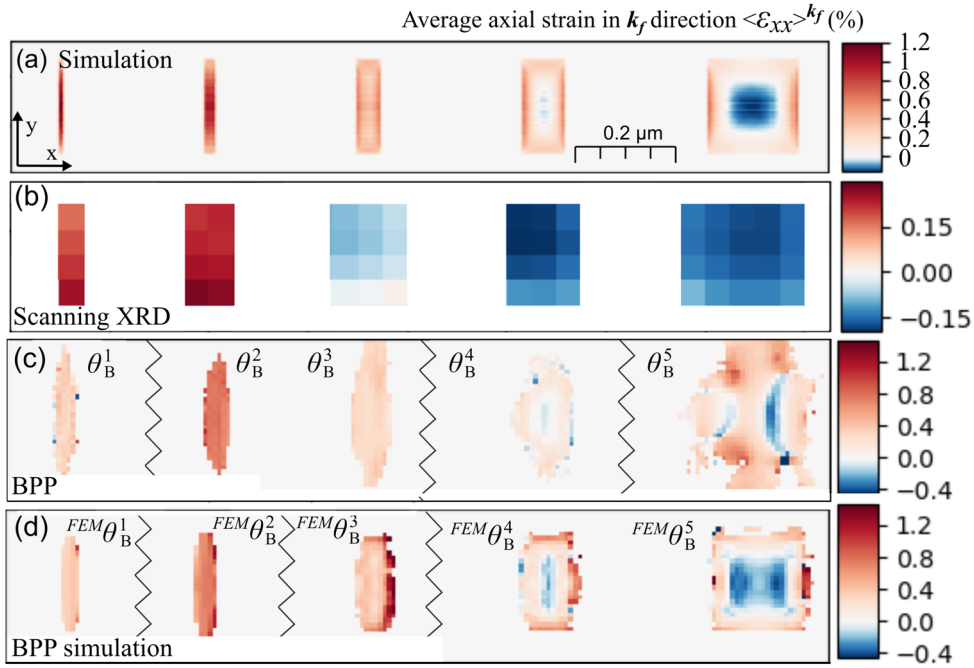

Figure 5.4 Strain mapping using BPP, compared to scanning XRD and finite element modelling. Adapted from paper II.

Generally, both methods show that the strain is highly dependent on segment length, in agreement with FEM. At the Bragg condition of an object, BPP reconstructs the object averaged over the $\boldsymbol{k}_f$ direction, if the approximation that there is little strain variation along $\boldsymbol{k}_f$ is valid. The averaging effect is less problematic for the smaller segments, which are strained more uniformly. However, the smallest segment has

weak scattering and a large extension in reciprocal space, making it harder to reconstruct with BPP as well as identifying the COM.

5.1.3 Finite element modelling

5.1.3.1 Setting up a finite element model in COMSOL

The initial strain distribution induced by the lattice mismatch in the nanowire was modelled using a model of linear elasticity. FEM can be used to simulate a wide range of physical systems that are governed by partial differential equations. The FEM is a numerical solution where the sample is discretised into a collection of elements, so that a solution to the partial differential equations can be iteratively approximated. The software COMSOL MULTIPHYSICS (version 5.4, COMSOL AB; Stockholm, Sweden) with the *solid mechanics* module was used for our simulations.

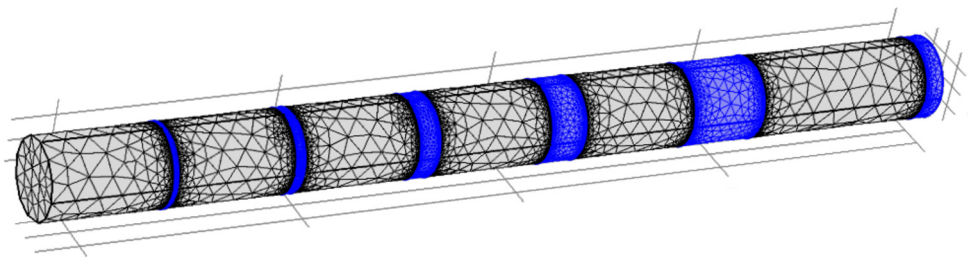

Figure 5.5 The mesh used in COMSOL for simulating the barcode structure with FEM.

In COMSOL, the geometry is first defined by drawing a realistic model of the sample in 3D. Here, the nanowire from paper I and II with five InP segments in a GaInP nanowire was drawn. Next, a mesh divides the geometry up into "finite elements", shown in Figure 5.5. For a 3D geometry, the mesh is made up of triangles, and the sizes are defined by the user with aid from the software. Finding a numerical solution with a small error take longer as the size gets smaller. To keep this balance right, areas in the geometry with high strain gradients were identified and smaller domains were used there for higher accuracy. Typical elements in the final version were about one nanometer.

The relevant material parameters for the linear elasticity model are density, Young's modulus and Poisson's ratio, all taken from Ref. [84]. The materials are defined as isotropic, i.e., the properties do not depend on the geometric direction. The lattice constants for pure InP and GaP were also found in Ref. [84], and the intermediate state $Ga_xIn_{1-x}P$ was calculated using Vegard's law. The same procedure was made for the Poisson's ratios, which is 0.36 for InP [84]. The lattice constants relationship is $a_{InP} > a_{GaInP}$. The displacement field is simulated based on a radial lattice

mismatch of 1.5%. Noe that the problem is not in 2D but 3D and that the initial strain is along two dimensions y and z.

5.1.3.2 Results from finite element modelling

The displacement field was recalculated to strain, as shown in Figure 5.6.

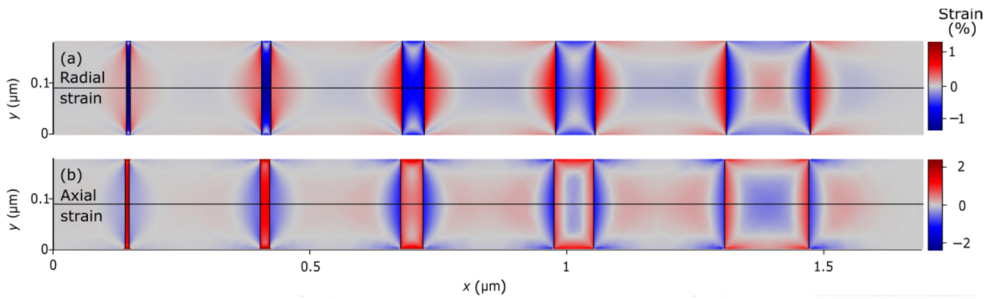

Figure 5.6 Radial (top) and axial (bottom) strain in a GaInP/InP heterostructured simulated with FEM. The strain comes from the lattice mismatch between GaInP and InP.

As expected from a linear elasticity model, the lattice expands axially where it is compressed radially and vice versa. The strain is high at the interface and at the sidewalls. A lot of the strain can be relaxed at the sidewall, which explains why it is easier to form a heterostructure of higher lattice mismatch in the nanowire form than in a planar geometry [6]. The strain at the interfaces has a complex dome shaped distribution in dome shapes. The trend is that the larger InP segments are more resilient to strain while the smaller segments are less so, and the smallest segment is almost completely adapted to the GaInP lattice. We observe in the GaInP segments, which are 265 nm in length, that the lattice is almost relaxed in their centers, more so as the InP insertions are shorter.

5.1.3.3 Nano-diffraction from a finite element model

A way to simulate nano-diffraction based on the COMSOL data was developed and used in paper I and II to simulate the scanning diffraction analysis and the BPP analysis, respectively. COMSOL outputs the displacement field inside the nanowire geometry as 3D scatter data. The experimental geometry sets up a numerical window in real space, which depends on the extension of the diffraction that is used, as well as the distance between the object and the detector. It is not determined by the focus size of the probe. The script creates a numerical box of complex numbers designating the nanowire, similar to the shape function in Eq. (2.24), but in discrete form. The amplitude is equal to integer one in the box and zero outside, and the phase is the displacement field times the scattering vector. Simulations of nano-XRD underpin the interpretation of the results. Using a plane wave enables interpretation of what part of the diffraction is coming from the sample, since a nanofocused probe itself will affect the Bragg peak. Figure 5.7 shows the simulated

diffraction from a single InP segment sandwiched between two GaInP segments, using a plane wave. The top row is from a 170 nm segment and the bottom row from a 80 nm segment. The Bragg peak is from the axial reflection, perpendicular to the lattice mismatch direction from the GaInP segments. In Figure 5.7 (a) and (c), the Bragg peak is proportional to the Fourier transform of the segment, shaped like a box. The finite size of the crystal gives the Bragg peaks their broadening. The square shape of the 170 nm segment is reflected in its square Bragg peak, while the shorter 80 nm segment is broader in q_1 (reciprocal to x). In Figure 5.7 (b) and (d), the displacement field is included in the simulation. This shifts the Bragg peak from the central symmetry and bends it in the direction of lower q_1 (to a higher lattice spacing). If the sign of the strain was reversed, the direction of the bending would be flipped, pointing towards higher q_1 values (and lower lattice spacing).

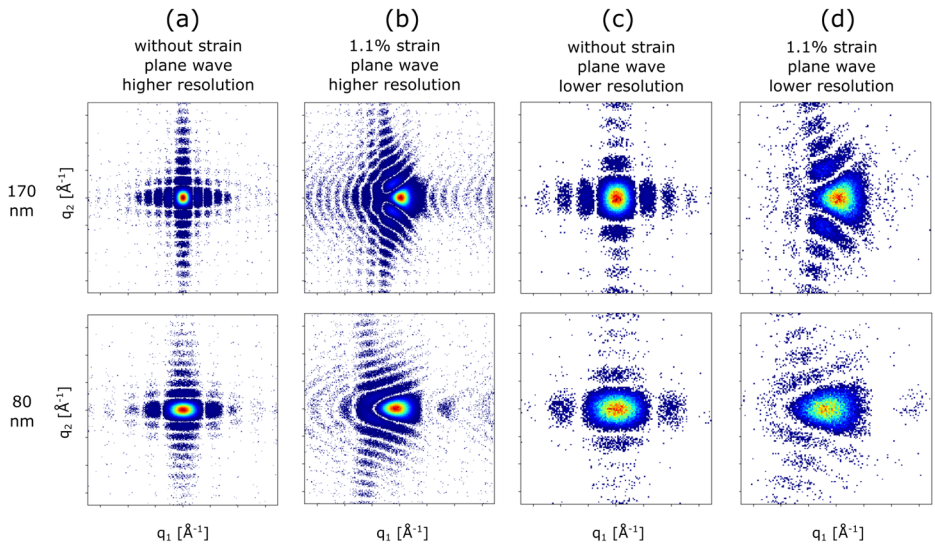

Figure 5.7 Simulated coherent diffraction patterns from a box of size 170 nm (top row) and 80 nm (bottom row) for four cases of strain and pixel size, where the lower resolution frames have larger pixel sizes.

5.2 Strain mapping of a nanowire device

Up to this point, we have been examining unprocessed nanowires. However, nanowires on their own are not particularly useful until they are integrated into a device. Here, X-ray beams are vital tools, as they are highly penetrating and can probe embedded objects. For a nanowire device, it is interesting to look at electrical measurements to probe the function of the device. X-ray beam induced current (XBIC) is a measure of the current induced in a device when exposed to X-rays. A detailed description of XBIC, and its results on nanowire devices, can be found in

Ref. [85]. The implementation of XBIC introduces a new contrast mode at the NanoMAX beamline, that can probe the local electronic properties and can be used in combination with already established techniques like XRF and XRD. XBIC can be used while the nanowire devices are in use, for example, to study local carrier dynamics under applied bias [86]. The system can be utilized for other various devices besides nanowires, such as transistors, light emitting diodes, or batteries.

In the first implementation, discussed in paper IV, we measure the strain and tilt in a contacted nanowire device using scanning XRD simultaneously with the XBIC signal, with XRF giving compositional information [87]. We probed the nanowire device using a 15 keV X-ray nanoprobe at the NanoMAX beamline, focused to 50 nm with the KB mirror setup. The nanowire device was connected to an amperemeter and a voltage source, that can be controlled and scripted with the same software that is controlling the motors in the setup.

For the experiment, a p-i-n doped InP solar cell nanowire device was formed by p-doping one end of the nanowire and n-doping the other, creating an excess of holes and electrons, respectively on each side. In the center, the free electrons and holes combine to form a neutral region, the *depletion region*. The nanowire was contacted by depositing gold on each end of the nanowire, forming a device. By measuring the XBIC signal, the number and origin of the electron-hole pairs that are induced by the X-rays can be established and the function of the device better understood [88].

Strain and tilt maps were created in the same way as previously described, and the result is shown in Figure 5.8 together with the XRD map. In Figure 5.8 (a), the XRF signal from the Au contacts are seen in blue and the In in the nanowire in green. The main cause of strain seen in Figure 5.8 (c) is the contacting, in line with previous experiments on nanowire devices [33] and FEM simulations of nanowire contacting [58]. From the strain map in Figure 5.8 (c), it is evident that the nanowire is compressively strained under the contacts but tensile strained in the center. This is evident from looking at the strain map and its correlation with the two tilt maps. The tilt profile in Figure 5.8 (e) indicates that the straining from the contact has caused the nanowire to bend so that the center of the nanowire is sticking out from the substrate, see also Ref. [33, 89]. The central part is strained and bent accordingly. The XBIC measurements from a nanowire on the same batch showed a clear current response from a region in the center of the nanowire, matching the position of the depletion region as expected.

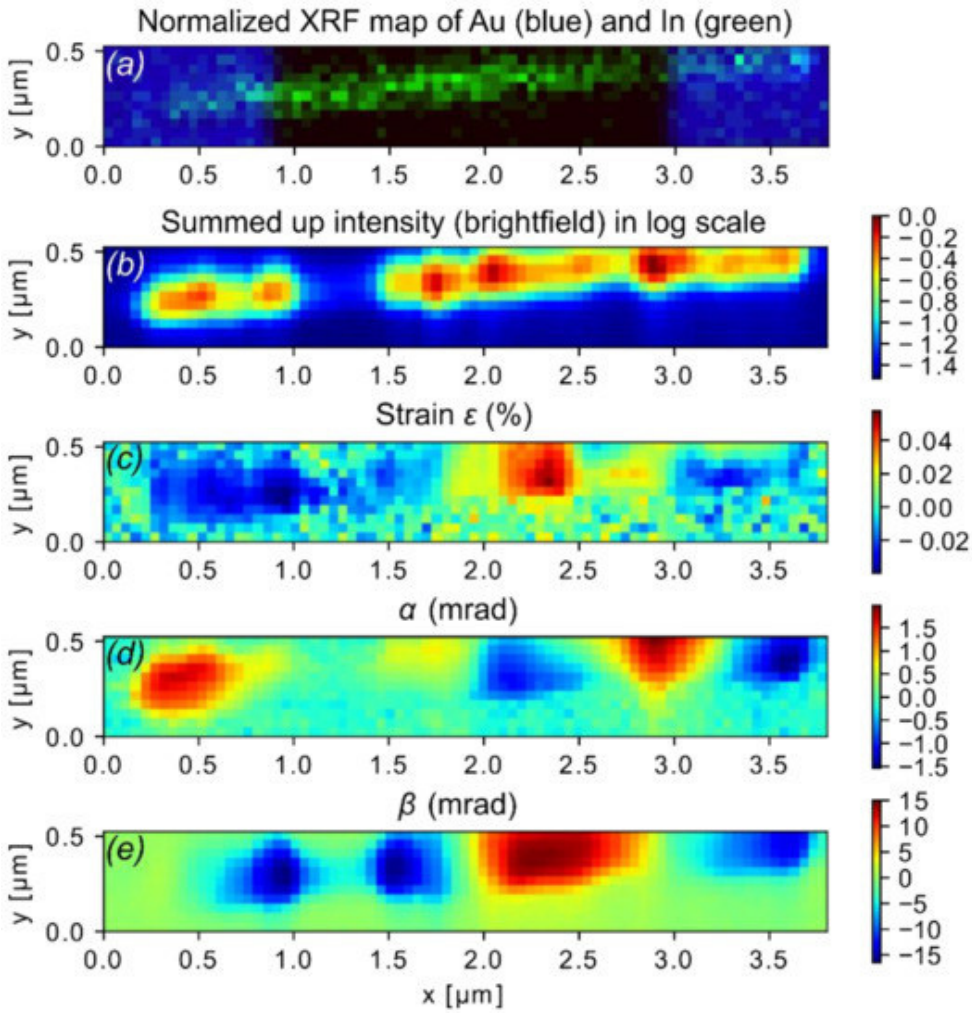

Figure 5.8. XRF and scanning XRD mapping of a p-i-n doped InP nanowire device.

5.3 Metal halide perovskite nanowires

Perovskite is a class of compounds with the chemical formula ABX_3, where A and B are positively charged ions (cations) and X is a negative ion (anion). They are explored for use in solar cells, since the power conversion efficiency (PCE) has undergone a staggering development with ten percentage points in ten years, reaching a PCE above 25% [90]. In metal halide perovskites (MHPs), the B is typically a metal (e.g., Pb, Sn or Ge) and X is an anion from the halide group (e.g.,

Cl^-, I^- and Br^-). MHPs has attracted a lot of attention and started an avalanche of research into applications such as light emitting diodes [91] and X-ray scintillators [92]. MHPs are generally a lot less sensitive to defects compared to the most common solar cell material Si. The development arose despite the materials problems with stability. MHPs are highly sensitive to exposure to air and moisture but the stability has seen improvements, from samples that are stable for only minutes to demonstrations of devices protected by capping layers that have 80% of their original efficiency after five years [93]. In paper III, we have taken a close look at newly fabricated MHP nanowire heterostructures, grown in our group, and address several open questions about composition, heterojunction formation and the ferroelastic nature that is often present in MHPs. We probe this with nanofocused synchrotron radiation using scanning diffraction and XRF mapping.

5.3.1 Samples

The $CsPbBr_3$ perovskite nanowire heterostructures are first grown as homogeneous $CsPbBr_3$ nanowires, and then processed into heterostructures. In the growth process, anodised aluminium oxide (AAO) is used as a template for the nanowires to grow inside [94]. The AAO has cylindrical pores inside, with diameters around 200 nm. The AAO is placed on a liquid solution with a CsBr and $PbBr_2$ precursor. Nanowires nucleate and grow inside the pores, and under the right conditions, they continue to grow as free-standing nanowires out from the AAO. The free-standing nanowires have an almost square cross section with lengths between 1 – 10 μm. The nanowires are removed from its substrate by scraping against the surface with a tissue, and subsequently transferred to a Si_3N_4 substrate.

The next step is to process the nanowires to create heterostructures. This is done by replacing some of the anions, the Br atoms, for Cl, in a selected part of the nanowire. This entails exposing parts of the nanowire to Cl in gas form, Cl_2, by coating the other half in a polymer. Some of the Br atoms are replaced with Cl and this creates a $CsPb(Br_{(1-x)}Cl_x)_3$ segment. The processing is described in detail in Ref. [95].

5.3.2 Ferroelasticity in MHP nanowires

A little background on ferroelasticity is needed in order to understand the results from the strain mapping. Ferroelastics are part of the family of properties that is sometimes referred to as ferroics, also including ferroelectrics and ferromagnetics. Of these, ferroelasticity has been proven in MHPs [96] and can potentially affect the performance of MHP nanowires.

In analogy to the electric dipole moment in a ferroelectric material, a ferroelastic material can exhibit a spontaneous strain. Commonly, crystals can undergo phase transitions to another stable crystal structure if they are subjected to external forces

like mechanical force or a change in temperature. A ferroelastic material is one that can undergo a ferroelastic phase transition, which involves changes in the shape of the unit cell. Following Ref. [97], the example of a cubic to tetragonal transition is explored. Here, the transition from cubic to tetragonal can occur by elongation of one of the axes to form a tetragonal phase. After a ferroelastic phase transition, several orientations of the new phase exist simultaneously. The different orientations occur in subareas of the crystal called *domains*. A ferroelastic phase transition is one that results in two or more such domains present in the crystal [97]. Of course, cubic to tetragonal is just an example and the concept can be generalised to other transitions.

The interface between two domains is called a *domain wall*, which usually occurs in a preferred crystal direction. The lattice mismatch between the domain walls is the "spontaneous strain" that was defined for a ferroelastic material. The domain formation can be induced by external forces e.g., mechanical force, temperature changes or strain [98], and can be either another crystal structure or a twin phase.

A phase transition may be different in bulk compared to in a nanocrystal. For instance, $CsPbBr_3$ is orthorhombic at room temperature (i.e., the unit cell basis vectors **a**, **b** and **c** have three distinct values and 90º angles between them) with a phase transition to tetragonal at 88ºC in bulk, but this has been reported to occur at 65ºC in nanocrystals [99].

5.3.3 Strain mapping and ferroelastic domains

In paper III, we present a study of $CsPbBr_3$ nanowires, probed with an X-ray beam focused to 60 x 60 nm at the NanoMAX beamline. Here, the (004) lattice planes, the planes orthogonal to the long axis of the nanowires, were probed with scanning XRD and the composition was mapped with XRF. We characterized both processed heterostructures and unprocessed reference nanowires and present the results from one of each. The main findings of paper III are described below.

The ends of the reference nanowire were slightly bent, and only the center of the nanowire is displayed in Figure 5.9 to present certain features more clearly. As expected from the reference nanowire, the XRF signal from Br, Pb and Cs are evenly distributed in the whole nanowire, see e.g., the Br signal in Figure 5.9 (a). The lattice spacing in Figure 5.9 (b) is also evenly distributed with an average value of d_{004} = 2.941Å. The α tilt, see Figure 5.9 (c), displays a weak gradient across the nanowire with a slightly positive tilt in the middle and slightly negative towards the ends. The most interesting result is seen in the β map, shown in Figure 5.9 (d), where around 500 nm long domains are observed, where the angle alternates between around ±0.2º in adjacent domains.

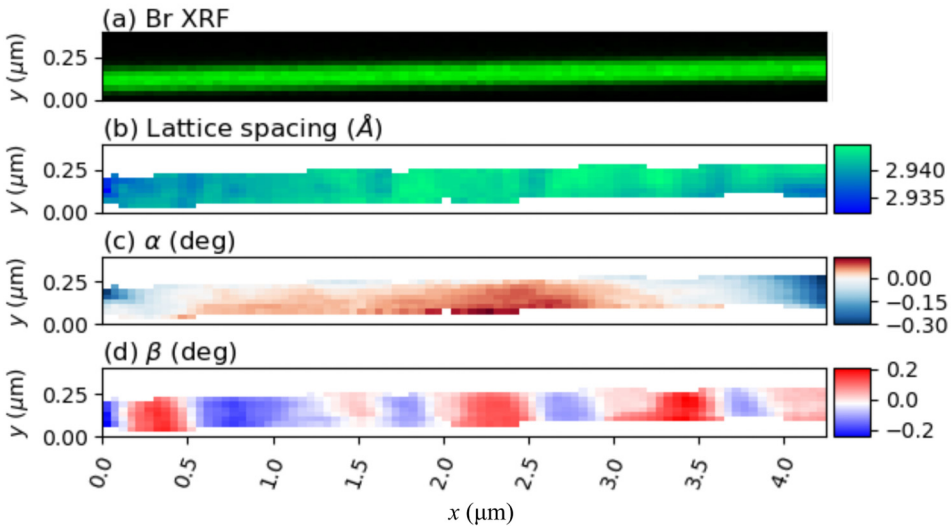

Figure 5.9. XRF and scanning XRD mapping of the center of a $CsPbBr_3$ reference nanowire. Adapted from paper III.

The XRF indicates a homogeneous composition in the reference nanowires, as expected. The lattice spacing is very close to the literature value 2.940 Å for the (004) lattice planes of the orthorhombic crystal structure, and is also in line with previously measured $CsPbBr_3$ nanowires [39]. When the lattice changes slowly on the length scale of the nanowire, the tilt variations could originate from bending of the nanowire, as for the α tilt in Figure 5.9 (b). For small, isolated areas, where the angle changes swiftly from one to the other, we instead assume that ferroelastic domains have formed. As there are no changes in lattice spacing that can be correlated with the variations in β, we interpreted this as a twin phase i.e., a domain with a different crystal orientation, where the domains are rotated around x with respect to each other.

Next, we investigated a heterostructured nanowire. The normalized XRF signals from Br (green) and Cl (blue) in the heterostructures nanowire are seen in Figure 5.10 (a). The left segment is the coated segment where the Br signal is prominent, and the left segment has been exposed to Cl. In the right segment, the signal from Br decreases drastically and we instead observe a stronger Cl signal. A sharp heterostructure interface is evident at approximately half of the nanowire, x = 2.5 μm, dividing the nanowire into two segments.

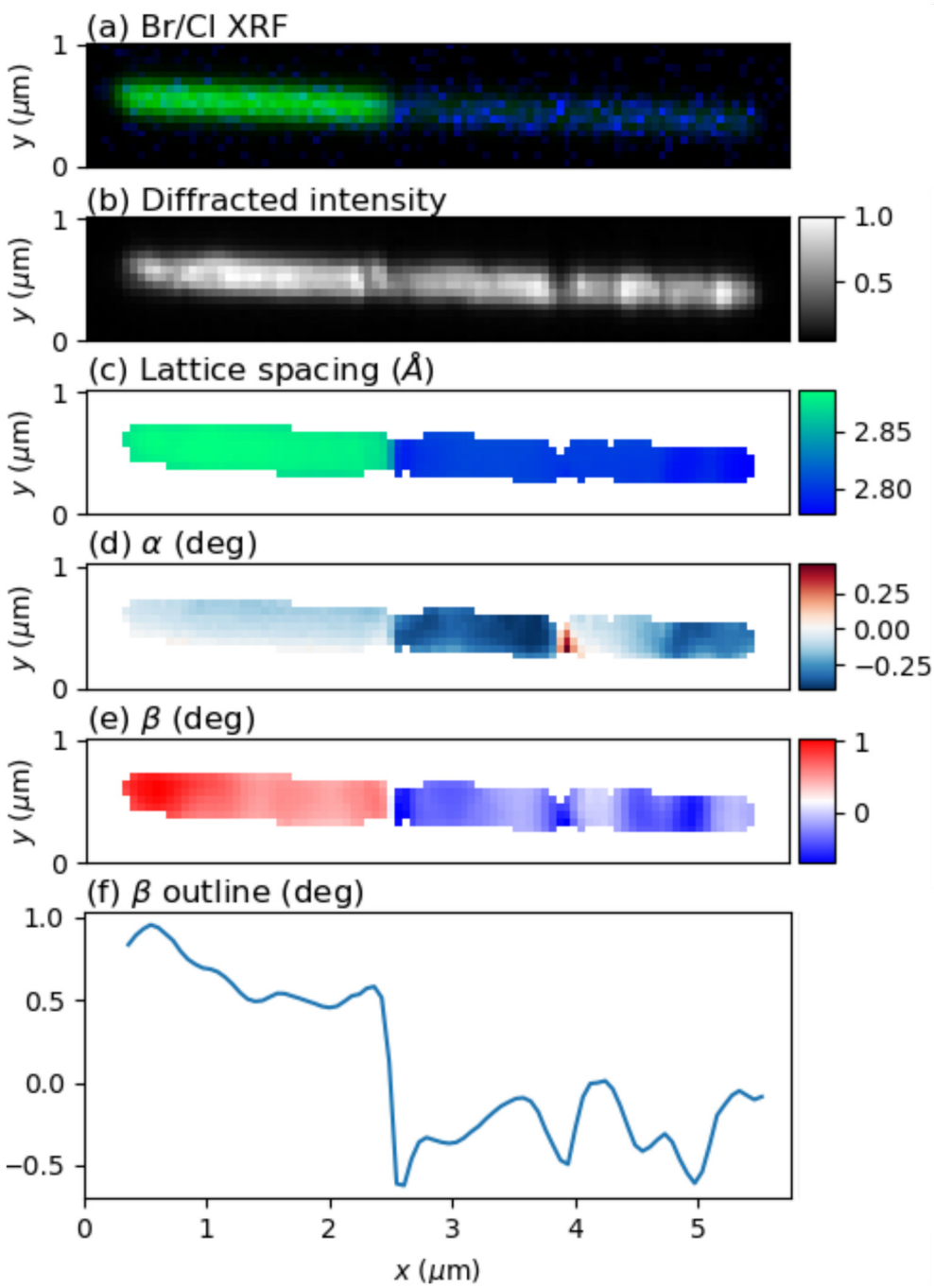

Figure 5.10. XRF and scanning XRD mapping of a $CsPbBr_3/CsPb(Br_{(1-x)}Cl_x)_3$ heterostructured nanowire. The segment to the left is $CsPbBr_3$, and the right side is processed to form $CsPb(Br_{(1-x)}Cl_x)_3$, which has a different lattice spacing.

The signature of a heterostructure is also seen in the lattice spacing map in Figure 5.10 (c). On average, the lattice spacing is d_{004} = 2.928 Å in the unchlorinated segment and d_{004} = 2.845 Å in the chlorinated segment. Within each segment, the lattice spacing is fairly homogeneous, with variations in the range of 0.04 Å. From the tilt maps, see α and β in Figure 5.10 (d-e), variations in crystal tilts between the unchlorinated and chlorinated segment are observed. In the β map on the chlorinated side, the angle repeatedly switches in the range of 0.5º.

The results from scanning XRD can also be used to calculate the quantitative composition of a material if the setup is properly calibrated. With the assumption that intermediate states can be estimated from pure $CsPbBr_3$ and pure $CsPbCl_3$ with a linear model, an estimate of the Cl concentrations can be found from the lattice spacing d_{004} using Vegard's law [87] for two materials A and B:

$$d_{A_{1-x}B_x} = (1-x)d_A + xd_B. \tag{5.1}$$

In the chlorinated segment, a 2.8% lower lattice spacing was observed compared to the unchlorinated. From this, we estimate the concentration of Cl to 66% in the chlorinated segment and 9% in the other.

We note from the XRF signal, including the Cs and Pb XRF signals not displayed here, that the nanowire is complete with no gaps or obvious damage. We also see that a heterostructure with a sharp interface has been successively formed. The lattice spacing in the unchlorinated segment was on average about 0.4% lower compared to the reference nanowire. This led us to take a closer look at the lattice spacing in the unchlorinated segment, and an axial gradient was observed across the segment, with a lower lattice spacing close to the heterojunction (i.e., higher ratio of Cl close to the interface). This indicates that some of the Cl molecules have diffused from the chlorinated side to the coated side of the nanowire. This could occur during or after the processing of the heterostructure, or both. The resolution was not sufficient to observe any radial gradient, which could be an additional migration process from under the coating to the nanowire center. Regarding the ferroelastic nature, the chlorinated segment indicates several ferroelastic domains, indicated by the rapid switches in β angle.

5.3.4 Conclusions

In conclusion, our characterization of MHP nanowires using scanning XRD and XRF with a nanofocused X-ray beam, showed complete nanowires with uniform composition, and the formation of heterostructures with a sharp interface. The results lead to a better understanding of the ion migration, implicating axial ion migration in the heterostructure, which is important feedback for the improvements of the heterostructure processing. Furthermore, our results indicate the occurrence of ferroelastic domains in the reference and heterostructured nanowires.

6 Summary and outlook

In summary, we have demonstrated that scanning nano X-ray diffraction using synchrotron radiation is a valuable technique for characterizing axial nanowire heterostructures and nanowire devices, demonstrated with a few examples in this thesis.

We have demonstrated results that resolve relative strain in III-V semiconductor axial heterostructured nanowires with 10^{-4} strain sensitivity and better than 100 nm spatial resolution. We saw that the strain distribution changed as a function of heterostructure segment length and correlated the results with FEM simulations. The largest segment had a complex distribution significantly different from bulk, with a large relaxation at the surface and a sign shift at its center. The interpretation of the results was facilitated by a FEM simulation, and we proved that, under some conditions, an elastic model of strain relaxation could effectively represent the behaviour of an axial heterostructure. The first ever X-ray scanning nano-diffraction from the beamline resulted in paper I.

Ptychography in the forward geometry was used to characterize the nanowires dimensions in experiments and the profile of the nanofocus. In Bragg geometry, we characterised variations in the lattice spacing using the 2D ptychographic technique in Bragg geometry, BPP. The high resolution phase maps were used to calculate strain maps and to validate a FEM model with high resolution.

The combination of scanning XRD, XRF and XBIC, enabled the mapping of strain composition and electric characteristics simultaneously, giving complementary results that facilitated the interpretation. This shows that the synchrotron radiation source allows for diverse experimental setups and sample environments.

Using nano-XRD on the perovskite nanowires in paper III, we addressed several open questions from the new type of $CsPbBr_3$ heterostructured nanowires; local information about composition, strain, and the ferroelastic nature of the nanowires. It was concluded that a sharp heterojunction had formed in the heterostructure and ferroelastic domains were revealed.

The most straightforward way to improve the spatial resolution in the nanowire strain maps is to reduce the focus size of the X-ray beam. State of the art is 10 nm or slightly below [100] but sub-5 nm focus has been demonstrated [3] using a multilayer zone plate. A drawback with using a more focused beam is the beam

damage that can be caused by a high flux in such a small focal spot. An alternative route towards higher resolution is coherent imaging, which simplifies the physical imaging system and enhances the resolution below the size of the beam using iterative algorithm to reconstruct the phase. On the other hand, longer measurement time is used which relates back to the issue of beam damage. Problems of stability have been a big obstacle for the progression of Bragg ptychography. Some remedy approaches include using a mixed-state approach that can account for incoherence and vibrations [101] and tuning the energy instead of rotating the sample [102, 103], or using interferometry to track the correct positions.

More synchrotron facilities around the world have or are planning to follow MAX IVs example and update to multibend achromats, such as the ESRF in France and NSLS II in the USA [104]. The increased brilliance this will achieve will be especially important for the development of coherent imaging methods.

References

1. Hÿtch, M.J. and A.M. Minor, Observing and measuring strain in nanostructures and devices with transmission electron microscopy. MRS bulletin, 2014. **39**(2): p. 138-146.
2. Schropp, A., R. Hoppe, J. Patommel, D. Samberg, F. Seiboth, S. Stephan, G. Wellenreuther, G. Falkenberg, and C.G. Schroer, Hard x-ray scanning microscopy with coherent radiation: Beyond the resolution of conventional x-ray microscopes. Applied Physics Letters, 2012. **100**(25): p. 253112.
3. Döring, F., A.L. Robisch, C. Eberl, M. Osterhoff, A. Ruhlandt, T. Liese, F. Schlenkrich, S. Hoffmann, M. Bartels, T. Salditt, et al., Sub-5 nm hard x-ray point focusing by a combined Kirkpatrick-Baez mirror and multilayer zone plate. Optics Express, 2013. **21**(16): p. 19311-19323.
4. Wallentin, J., N. Anttu, D. Asoli, M. Huffman, I. Åberg, M.H. Magnusson, G. Siefer, P. Fuss-Kailuweit, F. Dimroth, B. Witzigmann, et al., InP Nanowire Array Solar Cells Achieving 13.8% Efficiency by Exceeding the Ray Optics Limit. Science, 2013. **339**(6123): p. 1057.
5. Anttu, N., A. Abrand, D. Asoli, M. Heurlin, I. Åberg, L. Samuelson, and M. Borgström, Absorption of light in InP nanowire arrays. Nano Research, 2014. **7**(6): p. 816-823.
6. Glas, F., Chapter Two - Strain in Nanowires and Nanowire Heterostructures, in Semiconductors and Semimetals, A.F.I. Morral, S.A. Dayeh, and C. Jagadish, Editors. 2015, Elsevier. p. 79-123.
7. Röntgen, W.C., Uber eine neue Art von Strahlen. Sitzungsber Phys Med Ges Wurtzburg, 1895. **9**: p. 132-141.
8. Als-Nielsen, J., X-rays and matter – the basic interactions. Comptes Rendus Physique, 2008. **9**(5): p. 479-486.
9. Hermanns, C.F., X-ray absorption studies of metalloporphyrin molecules on surfaces: Electronic interactions, magnetic coupling, and chemical switches. 2013.
10. Hubbell, J.H., H.A. Gimm, and I. O/verbo/, Pair, triplet, and total atomic cross sections (and mass attenuation coefficients) for 1 MeV-100 GeV photons in elements Z= 1 to 100. Journal of physical and chemical reference data, 1980. **9**(4): p. 1023-1148.
11. Pavlinsky, G.V., Fundamentals of X-ray Physics. 2008: Cambridge International Science Publishing Ltd.
12. Paganin, D., Coherent X-ray optics. 2006: Oxford University Press on Demand.
13. Kittel, C., Introduction to solid state physics Eighth edition. 2021.

14. Stangl, J., C. Mocuta, V. Chamard, and D. Carbone, Nanobeam X-ray Scattering: Probing matter at the nanoscale. 2013: John Wiley & Sons.
15. Vartanyants, I.A. and I.K. Robinson, Partial coherence effects on the imaging of small crystals using coherent x-ray diffraction. Journal of Physics: Condensed Matter, 2001. **13**(47): p. 10593-10611.
16. v. Laue, M., Die äußere Form der Kristalle in ihrem Einfluß auf die Interferenzerscheinungen an Raumgittern. Annalen der Physik, 1936. **418**(1): p. 55-68.
17. Tavares, P.F., S.C. Leemann, M. Sjöström, and Å. Andersson, The MAX IV storage ring project. Journal of synchrotron radiation, 2014. **21**(5): p. 862-877.
18. Leemann, S.C. and W.A. Wurtz, Pushing the MAX IV 3 GeV storage ring brightness and coherence towards the limit of its magnetic lattice. Nuclear Instruments and Methods in Physics Research Section A: Accelerators, Spectrometers, Detectors and Associated Equipment, 2018. **884**: p. 92-96.
19. Als-Nielsen, J. and D. McMorrow, Elements of modern X-ray physics. 2011: John Wiley & Sons.
20. Eriksson, M., J.F. van der Veen, and C. Quitmann, Diffraction-limited storage rings–a window to the science of tomorrow. Journal of synchrotron radiation, 2014. **21**(5): p. 837-842.
21. Kirkpatrick, P. and A.V. Baez, Formation of optical images by X-rays. JOSA, 1948. **38**(9): p. 766-774.
22. Johansson, U., D. Carbone, S. Kalbfleisch, A. Björling, M. Kahnt, S. Sala, T. Stankevic, M. Liebi, A. Rodriguez Fernandez, and B. Bring, NanoMAX: the hard X-ray nanoprobe beamline at the MAX IV Laboratory. Journal of Synchrotron Radiation, 2021. **28**(6).
23. Li, P., M. Allain, T.A. Grünewald, M. Rommel, A. Campos, D. Carbone, and V. Chamard, 4th generation synchrotron source boosts crystalline imaging at the nanoscale. Light: Science & Applications, 2022. **11**(1): p. 73.
24. Björling, A., S. Kalbfleisch, M. Kahnt, S. Sala, K. Parfeniukas, U. Vogt, D. Carbone, and U. Johansson, Ptychographic characterization of a coherent nanofocused X-ray beam. Optics Express, 2020. **28**(4): p. 5069-5076.
25. Carbone, D., S. Kalbfleisch, U. Johansson, A. Bjorling, M. Kahnt, S. Sala, T. Stankevic, A. Rodriguez-Fernandez, B. Bring, Z. Matej, et al., Design and performance of a dedicated coherent X-ray scanning diffraction instrument at beamline NanoMAX of MAX IV. J Synchrotron Radiat, 2022. **29**(Pt 3): p. 876-887.
26. Warlo, M., G. Bark, C. Wanhainen, I. McElroy, A. Björling, and U. Johansson, Extreme-resolution synchrotron X-Ray fluorescence mapping of ore samples. Ore Geology Reviews, 2022. **140**: p. 104620.
27. Dupraz, M., G. Beutier, T.W. Cornelius, G. Parry, Z. Ren, S. Labat, M.-I. Richard, G.A. Chahine, O. Kovalenko, and M. De Boissieu, 3D imaging of a dislocation loop at the onset of plasticity in an indented nanocrystal. Nano letters, 2017. **17**(11): p. 6696-6701.

28. Kriegner, D., J.M. Persson, T. Etzelstorfer, D. Jacobsson, J. Wallentin, J.B. Wagner, K. Deppert, M. Borgström, and J. Stangl, Structural investigation of GaInP nanowires using X-ray diffraction. Thin Solid Films, 2013. **543**: p. 100-105.
29. Mandl, B., J. Stangl, T. Mårtensson, A. Mikkelsen, J. Eriksson, L.S. Karlsson, G. Bauer, L. Samuelson, and W. Seifert, Au-free epitaxial growth of InAs nanowires. Nano letters, 2006. **6**(8): p. 1817-1821.
30. Mino, L., E. Borfecchia, J. Segura-Ruiz, C. Giannini, G. Martinez-Criado, and C. Lamberti, Materials characterization by synchrotron x-ray microprobes and nanoprobes. Reviews of Modern Physics, 2018. **90**(2): p. 025007.
31. Biermanns, A., S. Breuer, A. Davydok, L. Geelhaar, and U. Pietsch, Structural polytypism and residual strain in GaAs nanowires grown on Si(111) probed by single-nanowire X-ray diffraction. Journal of Applied Crystallography, 2012. **45**(2): p. 239-244.
32. Stankevič, T., E. Hilner, F. Seiboth, R. Ciechonski, G. Vescovi, O. Kryliouk, U. Johansson, L. Samuelson, G. Wellenreuther, G. Falkenberg, et al., Fast Strain Mapping of Nanowire Light-Emitting Diodes Using Nanofocused X-ray Beams. ACS Nano, 2015. **9**(7): p. 6978-6984.
33. Wallentin, J., M. Osterhoff, and T. Salditt, In Operando X-Ray Nanodiffraction Reveals Electrically Induced Bending and Lattice Contraction in a Single Nanowire Device. Advanced Materials, 2016. **28**(9): p. 1788-1792.
34. Krause, T., M. Hanke, Z. Cheng, M. Niehle, A. Trampert, M. Rosenthal, M. Burghammer, J. Ledig, J. Hartmann, H. Zhou, et al., Nanofocus x-ray diffraction and cathodoluminescence investigations into individual core–shell (In,Ga)N/GaN rod light-emitting diodes. Nanotechnology, 2016. **27**(32): p. 325707.
35. Schülli, T.U. and S.J. Leake, X-ray nanobeam diffraction imaging of materials. Current Opinion in Solid State and Materials Science, 2018.
36. Chayanun, L., S. Hammarberg, H. Dierks, G. Otnes, A. Björling, M.T. Borgström, and J. Wallentin, Combining Nanofocused X-Rays with Electrical Measurements at the NanoMAX Beamline. Crystals, 2019. **9**(8): p. 432.
37. Marçal, L.A.B., E. Oksenberg, D. Dzhigaev, S. Hammarberg, A. Rothman, A. Björling, E. Unger, A. Mikkelsen, E. Joselevich, and J. Wallentin, In situ imaging of ferroelastic domain dynamics in CsPbBr3 perovskite nanowires by nanofocused scanning x-ray diffraction. ACS nano, 2020. **14**(11): p. 15973-15982.
38. Dzhigaev, D., J. Svensson, A. Krishnaraja, Z. Zhu, Z. Ren, Y. Liu, S. Kalbfleisch, A. Björling, F. Lenrick, and Z.I. Balogh, Strain mapping inside an individual processed vertical nanowire transistor using scanning X-ray nanodiffraction. Nanoscale, 2020. **12**(27): p. 14487-14493.
39. Marçal, L.A.B., S. Benter, A. Irish, D. Dzhigaev, E. Oksenberg, A. Rothman, E. Sanders, S. Hammarberg, Z. Zhang, S. Sala, et al., Inducing ferroelastic domains in single-crystal $CsPbBr_3$ perovskite nanowires using atomic force microscopy. Physical Review Materials, 2021. **5**(6).

40. Shin, J., T. Cornelius, S. Labat, F. Lauraux, M.-I. Richard, G. Richter, N. Blanchard, D. Gianola, and O. Thomas, In situ Bragg coherent X-ray diffraction during tensile testing of an individual Au nanowire. Journal of Applied Crystallography, 2018. **51**(3): p. 781-788.
41. Pelz, P.M., M. Guizar-Sicairos, P. Thibault, I. Johnson, M. Holler, and A. Menzel, On-the-fly scans for X-ray ptychography. Applied Physics Letters, 2014. **105**(25).
42. Sayre, D., Some implications of a theorem due to Shannon. Acta Crystallographica, 1952. **5**(6): p. 843-843.
43. Fienup, J.R., Reconstruction of an object from the modulus of its Fourier transform. Optics letters, 1978. **3**(1): p. 27-29.
44. Miao, J., P. Charalambous, J. Kirz, and D. Sayre, Extending the methodology of X-ray crystallography to allow imaging of micrometre-sized non-crystalline specimens. Nature, 1999. **400**: p. 342.
45. Fienup, J.R., Phase retrieval algorithms: a comparison. Applied optics, 1982. **21**(15): p. 2758-2769.
46. Rodenburg, J.M., A.C. Hurst, A.G. Cullis, B.R. Dobson, F. Pfeiffer, O. Bunk, C. David, K. Jefimovs, and I. Johnson, Hard-X-Ray Lensless Imaging of Extended Objects. Physical Review Letters, 2007. **98**(3): p. 034801.
47. Bunk, O., M. Dierolf, S. Kynde, I. Johnson, O. Marti, and F. Pfeiffer, Influence of the overlap parameter on the convergence of the ptychographical iterative engine. Ultramicroscopy, 2008. **108**(5): p. 481-487.
48. Rodenburg, J.M. and H.M. Faulkner, A phase retrieval algorithm for shifting illumination. Applied physics letters, 2004. **85**(20): p. 4795-4797.
49. Maiden, A.M. and J.M. Rodenburg, An improved ptychographical phase retrieval algorithm for diffractive imaging. Ultramicroscopy, 2009. **109**(10): p. 1256-1262.
50. Thibault, P., M. Dierolf, A. Menzel, O. Bunk, C. David, and F. Pfeiffer, High-resolution scanning x-ray diffraction microscopy. Science, 2008. **321**(5887): p. 379-382.
51. Thibault, P., M. Dierolf, O. Bunk, A. Menzel, and F. Pfeiffer, Probe retrieval in ptychographic coherent diffractive imaging. Ultramicroscopy, 2009. **109**(4): p. 338-343.
52. Robinson, I.K., I.A. Vartanyants, G. Williams, M. Pfeifer, and J. Pitney, Reconstruction of the shapes of gold nanocrystals using coherent x-ray diffraction. Physical review letters, 2001. **87**(19): p. 195505.
53. Robinson, I. and R. Harder, Coherent X-ray diffraction imaging of strain at the nanoscale. Nature Materials, 2009. **8**: p. 291.
54. Pfeifer, M.A., G.J. Williams, I.A. Vartanyants, R. Harder, and I.K. Robinson, Three-dimensional mapping of a deformation field inside a nanocrystal. Nature, 2006. **442**: p. 63.
55. Newton, M.C., S.J. Leake, R. Harder, and I.K. Robinson, Three-dimensional imaging of strain in a single ZnO nanorod. Nature Materials, 2010. **9**(2): p. 120-124.

56. Diaz, A., C. Mocuta, J. Stangl, B. Mandl, C. David, J. Vila-Comamala, V. Chamard, T.H. Metzger, and G. Bauer, Coherent diffraction imaging of a single epitaxial InAs nanowire using a focused x-ray beam. Physical Review B, 2009. **79**(12): p. 125324.
57. Dzhigaev, D., A. Shabalin, T. Stankevič, U. Lorenz, R.P. Kurta, F. Seiboth, J. Wallentin, A. Singer, S. Lazarev, O.M. Yefanov, et al., Bragg coherent x-ray diffractive imaging of a single indium phosphide nanowire. Journal of Optics, 2016. **18**(6): p. 064007.
58. Lazarev, S., D. Dzhigaev, Z. Bi, A. Nowzari, Y.Y. Kim, M. Rose, I.A. Zaluzhnyy, O.Y. Gorobtsov, A.V. Zozulya, F. Lenrick, et al., Structural Changes in a Single GaN Nanowire under Applied Voltage Bias. Nano Lett, 2018.
59. Hill, M.O., P. Schmiedeke, C. Huang, S. Maddali, X. Hu, S.O. Hruszkewycz, J.J. Finley, G. Koblmüller, and L.J. Lauhon, 3D Bragg Coherent Diffraction Imaging of Extended Nanowires: Defect Formation in Highly Strained InGaAs Quantum Wells. ACS Nano, 2022.
60. Godard, P., G. Carbone, M. Allain, F. Mastropietro, G. Chen, L. Capello, A. Diaz, T.H. Metzger, J. Stangl, and V. Chamard, Three-dimensional high-resolution quantitative microscopy of extended crystals. Nature Communications, 2011. **2**: p. 568.
61. Chamard, V., M. Allain, P. Godard, A. Talneau, G. Patriarche, and M. Burghammer, Strain in a silicon-on-insulator nanostructure revealed by 3D x-ray Bragg ptychography. Scientific reports, 2015. **5**: p. 9827.
62. Pateras, A.I., M. Allain, P. Godard, L. Largeau, G. Patriarche, A. Talneau, K. Pantzas, M. Burghammer, A.A. Minkevich, and V. Chamard, Nondestructive three-dimensional imaging of crystal strain and rotations in an extended bonded semiconductor heterostructure. Physical Review B, 2015. **92**(20): p. 205305.
63. Li, P., N.W. Phillips, S. Leake, M. Allain, F. Hofmann, and V. Chamard, Revealing nano-scale lattice distortions in implanted material with 3D Bragg ptychography. Nature Communications, 2021. **12**(1): p. 7059.
64. Hruszkewycz, S.O., M.V. Holt, C.E. Murray, J. Bruley, J. Holt, A. Tripathi, O.G. Shpyrko, I. McNulty, M.J. Highland, and P.H. Fuoss, Nano Lett., 2012. **12**: p. 5148.
65. Holt, M.V., S.O. Hruszkewycz, C.E. Murray, J.R. Holt, D.M. Paskiewicz, and P.H. Fuoss, Strain imaging of nanoscale semiconductor heterostructures with x-ray Bragg projection ptychography. Phys Rev Lett, 2014. **112**(16): p. 165502.
66. Dzhigaev, D., T. Stankevič, Z. Bi, S. Lazarev, M. Rose, A. Shabalin, J. Reinhardt, A. Mikkelsen, L. Samuelson, G. Falkenberg, et al., X-ray bragg ptychography on a single InGaN/GaN core–shell nanowire. ACS nano, 2017. **11**(7): p. 6605-6611.
67. Hruszkewycz, S.O., M. Allain, M.V. Holt, C.E. Murray, J.R. Holt, P.H. Fuoss, and V. Chamard, High-resolution three-dimensional structural microscopy by single-angle Bragg ptychography. Nat Mater, 2017. **16**(2): p. 244-251.
68. Hill, M.O., I. Calvo-Almazan, M. Allain, M.V. Holt, A. Ulvestad, J. Treu, G. Koblmuller, C. Huang, X. Huang, H. Yan, et al., Measuring Three-Dimensional Strain and Structural Defects in a Single InGaAs Nanowire Using Coherent X-ray Multiangle Bragg Projection Ptychography. Nano Lett, 2018. **18**(2): p. 811-819.

69. Hruszkewycz, S.O., Q. Zhang, M.V. Holt, M.J. Highland, P.G. Evans, and P.H. Fuoss, Structural sensitivity of x-ray Bragg projection ptychography to domain patterns in epitaxial thin films. Physical Review A, 2016. **94**(4): p. 043803.
70. Dzhigaev, D., T. Stankevič, I. Besedin, S. Lazarev, A. Shabalin, M.N. Strikhanov, R. Feidenhans'l, and I.A. Vartanyants, Theoretical analysis of the strain mapping in a single core-shell nanowire by x-ray Bragg ptychography. SPIE Optical Engineering + Applications. Vol. 9592. 2015: SPIE.
71. Geisz, J.F., R.M. France, K.L. Schulte, M.A. Steiner, A.G. Norman, H.L. Guthrey, M.R. Young, T. Song, and T. Moriarty, Six-junction III–V solar cells with 47.1% conversion efficiency under 143 Suns concentration. Nature energy, 2020. **5**(4): p. 326-335.
72. Haverkort, J.E.M., E.C. Garnett, and E.P.A.M. Bakkers, Fundamentals of the nanowire solar cell: Optimization of the open circuit voltage. Applied Physics Reviews, 2018. **5**(3): p. 031106.
73. Otnes, G. and M.T. Borgström, Towards high efficiency nanowire solar cells. Nano Today, 2017. **12**: p. 31-45.
74. Gudiksen, M.S., L.J. Lauhon, J. Wang, D.C. Smith, and C.M. Lieber, Growth of nanowire superlattice structures for nanoscale photonics and electronics. Nature, 2002. **415**: p. 617.
75. Gibson, S.J., B. van Kasteren, B. Tekcan, Y. Cui, D. van Dam, J.E. Haverkort, E.P. Bakkers, and M.E. Reimer, Tapered InP nanowire arrays for efficient broadband high-speed single-photon detection. Nature nanotechnology, 2019. **14**(5): p. 473.
76. Barrigón, E., M. Heurlin, Z. Bi, B. Monemar, and L. Samuelson, Synthesis and Applications of III–V Nanowires. Chemical Reviews, 2019. **119**(15): p. 9170-9220.
77. Motohisa, J., H. Kameda, M. Sasaki, and K. Tomioka, Characterization of nanowire light-emitting diodes grown by selective-area metal-organic vapor-phase epitaxy. Nanotechnology, 2019. **30**(13): p. 134002.
78. Memisevic, E., M. Hellenbrand, E. Lind, A.R. Persson, S. Sant, A. Schenk, J. Svensson, R. Wallenberg, and L.-E. Wernersson, Individual Defects in InAs/InGaAsSb/GaSb Nanowire Tunnel Field-Effect Transistors Operating below 60 mV/decade. Nano Letters, 2017. **17**(7): p. 4373-4380.
79. Tomioka, K., M. Yoshimura, and T. Fukui, A III–V nanowire channel on silicon for high-performance vertical transistors. Nature, 2012. **488**: p. 189.
80. Jia, C., Z. Lin, Y. Huang, and X. Duan, Nanowire electronics: From nanoscale to macroscale. Chemical reviews, 2019. **119**(15): p. 9074-9135.
81. Memisevic, E., J. Svensson, E. Lind, and L.E. Wernersson, Vertical Nanowire TFETs With Channel Diameter Down to 10 nm and Point SMIN of 35 mV/Decade. IEEE Electron Device Letters, 2018. **39**(7): p. 1089-1091.
82. Hrachowina, L., Y. Chen, E. Barrigon, R. Wallenberg, and M.T. Borgström, Realization of axially defined GaInP/InP/InAsP triple-junction photovoltaic nanowires for high performance solar cells. Materials Today Energy, 2022: p. 101050.
83. Enders, B. and P. Thibault, A computational framework for ptychographic reconstructions. Proc Math Phys Eng Sci, 2016. **472**(2196): p. 20160640.

84. Ioffe. Ioffe Institute Physical Properties of Semiconductors Electronic Archive. May, 2017]; Available from: http://www.ioffe.ru/SVA/NSM/Semicond/index.html.
85. Chayanun, L., Nanowire devices for X-ray detection. 2020, Lund University.
86. Zapf, M., M. Ritzer, L. Liborius, A. Johannes, M. Hafermann, S. Schönherr, J. Segura-Ruiz, G. Martínez-Criado, W. Prost, and C. Ronning, Hot electrons in a nanowire hard X-ray detector. Nature Communications, 2020. **11**(1): p. 4729.
87. Segura-Ruiz, J., G. Martínez-Criado, M.H. Chu, S. Geburt, and C. Ronning, Nano-X-ray Absorption Spectroscopy of Single Co-Implanted ZnO Nanowires. Nano Letters, 2011. **11**(12): p. 5322-5326.
88. Chayanun, L., G. Otnes, A. Troian, S. Hammarberg, D. Salomon, M.T. Borgstrom, and J. Wallentin, Nanoscale mapping of carrier collection in single nanowire solar cells using X-ray beam induced current. Journal of Synchrotron Radiation, 2019. **26**(1).
89. Wallentin, J., D. Jacobsson, M. Osterhoff, M.T. Borgstrom, and T. Salditt, Bending and Twisting Lattice Tilt in Strained Core-Shell Nanowires Revealed by Nanofocused X-ray Diffraction. Nano Lett, 2017. **17**(7): p. 4143-4150.
90. Best Research-Cell Efficiencies Chart-NREL. *https://www.nrel.gov/pv/cell-efficiency.html* 2023.
91. Liu, X.-K., W. Xu, S. Bai, Y. Jin, J. Wang, R.H. Friend, and F. Gao, Metal halide perovskites for light-emitting diodes. Nature Materials, 2021. **20**(1): p. 10-21.
92. Chen, Q., J. Wu, X. Ou, B. Huang, J. Almutlaq, A.A. Zhumekenov, X. Guan, S. Han, L. Liang, Z. Yi, et al., All-inorganic perovskite nanocrystal scintillators. Nature, 2018. **561**(7721): p. 88-93.
93. Zhao, X., T. Liu, Q.C. Burlingame, T. Liu, R. Holley, G. Cheng, N. Yao, F. Gao, and Y.-L. Loo, Accelerated aging of all-inorganic, interface-stabilized perovskite solar cells. Science, 2022. **377**(6603): p. 307-310.
94. Zhang, Z., N. Lamers, C. Sun, C. Hetherington, I.G. Scheblykin, and J. Wallentin, *Free-Standing Metal Halide Perovskite Nanowire Arrays with Blue-Green Heterostructures.* Nano Letters, 2022. **22**(7): p. 2941-2947.
95. Lamers, N., Z. Zhang, I.G. Scheblykin, and J. Wallentin, *Multisegment Heterostructured $CsPb(Br_{1-x}Cl_x)_3$ Perovskite Nanowires using Gas-Phase Anion Exchange.* **In review**, 2023.
96. Frost, J.M., K.T. Butler, F. Brivio, C.H. Hendon, M. Van Schilfgaarde, and A. Walsh, *Atomistic origins of high-performance in hybrid halide perovskite solar cells.* Nano letters, 2014. **14**(5): p. 2584-2590.
97. Wadhawan, V., *Introduction to ferroic materials*. 2000: CRC press.
98. Salje, E.K., *Ferroelastic materials.* Annual Review of Materials Research, 2012. **42**: p. 265-283.
99. Kirschner, M.S., B.T. Diroll, P. Guo, S.M. Harvey, W. Helweh, N.C. Flanders, A. Brumberg, N.E. Watkins, A.A. Leonard, A.M. Evans, et al., *Photoinduced, reversible phase transitions in all-inorganic perovskite nanocrystals.* Nature Communications, 2019. **10**(1): p. 504.

100. Mimura, H., S. Handa, T. Kimura, H. Yumoto, D. Yamakawa, H. Yokoyama, S. Matsuyama, K. Inagaki, K. Yamamura, and Y. Sano, *Breaking the 10 nm barrier in hard-X-ray focusing.* Nature physics, 2010. **6**(2): p. 122-125.
101. Thibault, P. and A. Menzel, *Reconstructing state mixtures from diffraction measurements.* Nature, 2013. **494**(7435): p. 68-71.
102. Cornelius, T., D. Carbone, V. Jacques, T. Schülli, and T. Metzger, *Three-dimensional diffraction mapping by tuning the X-ray energy.* Journal of synchrotron radiation, 2011. **18**(3): p. 413-417.
103. Cha, W., A. Ulvestad, M. Allain, V. Chamard, R. Harder, S.J. Leake, J. Maser, P.H. Fuoss, and S.O. Hruszkewycz, *Three Dimensional Variable-Wavelength X-Ray Bragg Coherent Diffraction Imaging.* Physical Review Letters, 2016. **117**(22): p. 225501.
104. Eriksson, M. *The multi-bend achromat storage rings*. in *AIP Conference Proceedings*. 2016. AIP Publishing LLC.

Printed by Media-Tryck, Lund 2023 NORDIC SWAN ECOLABEL 3041 0903

ISBN 978-91-8039-653-0
Division of Synchrotron Radiation Research
Department of Physics
Faculty of Science
Lund University